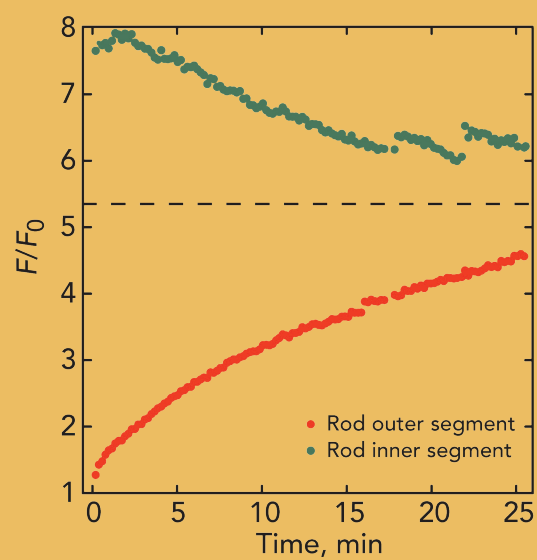
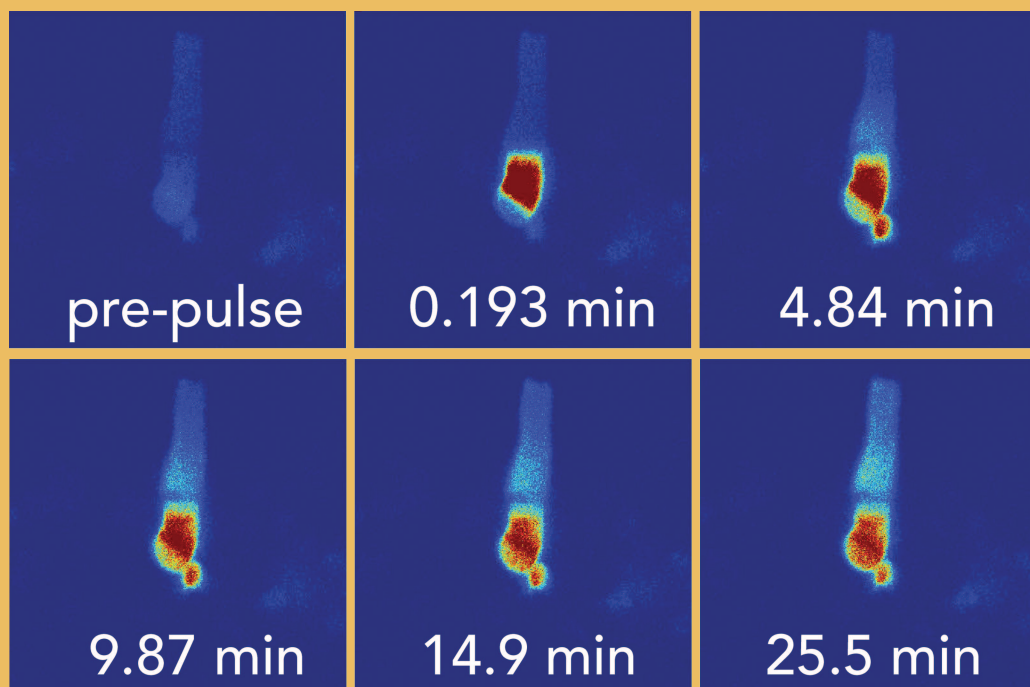


JGP

The Journal of General Physiology

Vol 135 • No 3 • March 2010



Diffusion of a soluble protein, photoactivatable GFP, through a sensory cilium

Peter D. Calvert,^{1,2} William E. Schiesser,³ and Edward N. Pugh Jr.⁴

¹Department of Ophthalmology and ²Department of Biochemistry and Molecular Biology, SUNY Upstate Medical University, Syracuse, NY 13210

³Department of Chemical Engineering, Lehigh University, Bethlehem, PA 18015

⁴Department of Physiology, University of California, Davis, Davis, CA 95616

Transport of proteins to and from cilia is crucial for normal cell function and survival, and interruption of transport has been implicated in degenerative and neoplastic diseases. It has been hypothesized that the ciliary axoneme and structures adjacent to and including the basal bodies of cilia impose selective barriers to the movement of proteins into and out of the cilium. To examine this hypothesis, using confocal and multiphoton microscopy we determined the mobility of the highly soluble photoactivatable green fluorescent protein (PAGFP) in the connecting cilium (CC) of live *Xenopus* retinal rod photoreceptors, and in the contiguous subcellular compartments bridged by the CC, the inner segment (IS) and the outer segment (OS). The estimated axial diffusion coefficients are $D_{CC} = 2.8 \pm 0.3$, $D_{IS} = 5.2 \pm 0.6$, and $D_{OS} = 0.079 \pm 0.009 \mu\text{m}^2 \text{s}^{-1}$. The results establish that the CC does not pose a major barrier to protein diffusion within the rod cell. However, the results also reveal that axial diffusion in each of the rod's compartments is substantially retarded relative to aqueous solution: the axial diffusion of PAGFP was retarded ~ 18 -, 32- and 1,000-fold in the IS, CC, and OS, respectively, with ~ 20 -fold of the reduction in the OS attributable to tortuosity imposed by the lamellar disc membranes. Previous investigation of PAGFP diffusion in passed, spherical Chinese hamster ovary cells yielded $D_{CHO} = 20 \mu\text{m}^2 \text{s}^{-1}$, and estimating cytoplasmic viscosity as $D_{aq}/D_{CHO} = 4.5$, the residual 3- to 10-fold reduction in PAGFP diffusion is ascribed to sub-optical resolution structures in the IS, CC, and OS compartments.

INTRODUCTION

Cilia are evolutionarily conserved subcellular organelles present on most cells of the body, and they serve many essential physiological functions, including vision, hearing, olfaction, and mechanosensation (Davis et al., 2006). The functions of many cilia remain undetermined, yet their importance is evident from the fact that mutations in genes encoding ciliary proteins give rise to devastating hereditary and often multi-organ disease, including Bardet-Biedl syndrome, Usher syndrome, combined polycystic kidney disease, and retinal degeneration (Pazour and Rosenbaum, 2002; Badano et al., 2006). Thus, a quantitative understanding of cilia construction, maintenance, and function is important for cell biology, physiology, and medicine.

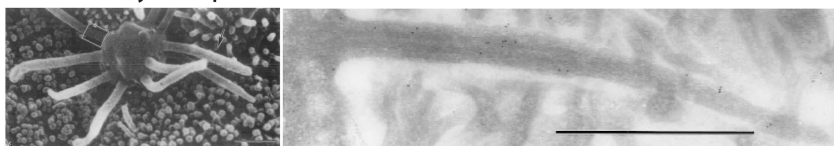
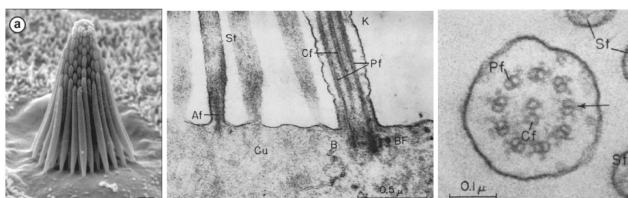
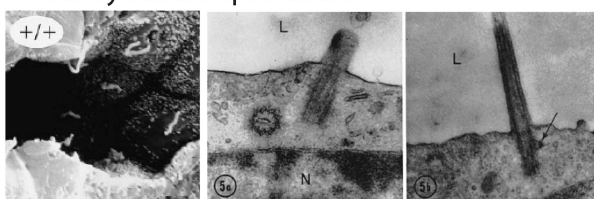
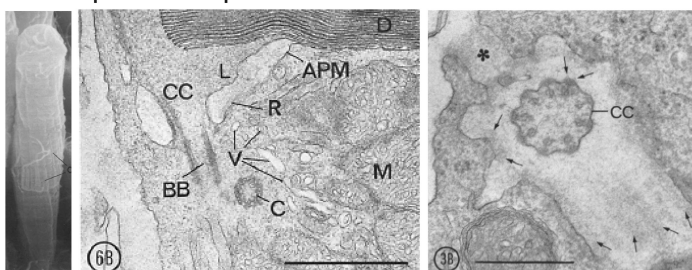
All cilia are organized around a microtubule-based axoneme that is surrounded by a plasma membrane specialized with tissue-specific molecular sensors and ion channels (Fig. 1). The axoneme extends from and is anchored to basal bodies consisting of the centrioles

that organize the cytoskeleton of the ciliary axoneme and of the spindle apparatus during cell division. Recent proteomic analysis of primary cilia shows that they comprise several hundred (Blacque et al., 2005; Pazour et al., 2005) to a couple of thousand proteins (Liu et al., 2007), depending on the species. Cilia do not contain protein and membrane synthetic machinery; thus, a central problem in the study of cilia has been to determine the mode of delivery of proteins to and removal from this relatively isolated compartment.

A distinctive form of molecular motor transport, intraflagellar transport (IFT), is a hallmark of primary cilia (Rosenbaum and Witman, 2002). Originally discovered in *Chlamydomonas* (Kozminski et al., 1995), IFT is highly conserved in eukaryotes, involving kinesin and dynein-based transport of large, multi-molecular particles along the microtubules of the ciliary axoneme (Rosenbaum and Witman, 2002). IFT transport has been proposed to subserve the coordinated delivery of both nonmembrane-bound and membrane-bound molecular components to, and their removal from, the cilium, allowing it to grow and be renewed, despite its removal from the

Correspondence to Peter D. Calvert: calvertp@upstate.edu

Abbreviations used in this paper: BC, boundary condition; CC, connecting cilium; CHO, Chinese hamster ovary; EFGP, enhanced green fluorescent protein; EM, electron micrograph; IFT, intraflagellar transport; IS, inner segment; ODE, ordinary differential equation; OS, outer segment; PAGFP, photoactivatable green fluorescent protein; ROI, region of interest.

A Olfactory receptor**B Hair cell****C Kidney tubule epithelium****D Rod photoreceptor**

the retina are modified cilia that transduce light into visual signals. The OSs contain opsin molecules that absorb photons and pass the light signal down a transduction cascade that leads to channel closure in the plasma membrane. Mutations in ciliary genes lead to retinal degeneration and blindness, such as in retinitis pigmentosa. (Left) Scanning EM of a frog rod. (Middle) Longitudinal section through the CC showing the basal body and the associated centriole. Note the lamellar discs (D) of the OS and the mitochondria (M) of the IS compartments. Bar, 1 μ m. (Right) Cross section of the CC just distal to the basal body. Bar, 0.5 μ m. Images reproduced from Peters et al. (1983) with permission.

nucleus, ER, and Golgi. A hypothesis implicit in the proposed function of IFT is that both the membrane and the interior of the cilium are effectively separated from the plasma membrane and cytoplasm of the cell body. Indeed, it has been explicitly proposed that the basal bodies and the associated structures at the base of the cilium, including the transitional fibers that extend to the plasma membrane, provide either sieving mechanisms that limit the size of soluble molecules allowed to pass into and out of cilia to ~ 10 kD (Jensen et al., 2004; Praetorius and Spring, 2005), or serve as a gating mechanism that controls the passage of proteins between the ciliary compartment and the bulk cytoplasm (Deane et al., 2001; Trojan et al., 2008). Moreover, parallels have been drawn between the basal body complex and nuclear pore complexes in terms of control of protein

Figure 1. Ultrastructures of a sampling of primary cilia. (A) Olfactory receptor cilia contain the molecular machinery of odorant transduction. Defects in ciliary genes lead to anosmia (Kulaga et al., 2004). (Left) Scanning EM of an embryonic rat olfactory receptor dendritic knob with multiple primary cilia (reproduced from Menco, 1997 with permission of Oxford University Press). (Right) Longitudinal section through an olfactory cilium (reproduced from Menco et al., 1997 [fig. 6] with permission from Springer Science and Business Media). Bar, 1 μ m. (B) Hair cells are mechanoreceptors. They generally have only one true cilium, the kinocilium, the longest structure found at the back of the ciliary bundle. Defects in ciliary genes lead to reduced hearing and deafness, such as in Usher's syndrome. (Left) Scanning EM of stereocilia from a frog saccule (reproduced from Vollrath et al., 2007 with permission). Bar, 1 μ m. (Middle and right) Sections through the kinocilia of teleost fish (reproduced from Flock and Duvall, 1965 with permission). (Middle) Longitudinal section through the kinocilium base. Bar, 0.5 μ m. (Right) Cross section showing a 9 + 2 axonemal structure. Bar, 0.1 μ m. (C) Kidney tubule epithelial cells possess single cilia, whose function remains unknown, but it has been proposed that they serve some sensory role, such as the detection of fluid flow. Mutations in cilia genes lead to polycystic kidney disease and loss of renal function. (Left) Scanning EM of mouse kidney tubule epithelial cells showing several cilia projecting into the lumen (Pazour et al., 2000). (Middle and right) Longitudinal sections through the base of the cilia showing the basal body and centriole (reproduced from Ganote et al., 1968 with permission). (D) Photoreceptors in

permeability (Deane et al., 2001). These proposals rest primarily on ultrastructural studies of cilia and flagella and on studies where IFT components have been genetically ablated or reduced, resulting in shortening, disorganization, or complete loss of the cilia or flagella. However, the structure of the primary cilium (Fig. 1), with its apparently patent central core, suggests that the cilium may not be isolated from the bulk cytoplasm and that a mode of transport distinct from IFT, namely diffusion, could also be available for transport of soluble proteins within cilia.

Here, for the first time, we report measurements of the diffusion of a soluble protein within a primary cilium, the connecting cilium (CC) of retinal rod photoreceptor. Photoreceptors provide both a rationale and a useful preparation for the investigation of diffusional

movement of proteins in primary cilia. A rationale comes from the massive light-dependent translocation of soluble phototransduction proteins, including arrestin (~ 48 kD), transducin (α subunit, ~ 39 kD; $\beta\gamma$, ~ 46 kD), and recoverin (~ 23 kD) between the inner segment (IS) and outer segment (OS) compartments of rods (Broekhuyse et al., 1985; Philp et al., 1987; Peet et al., 2004; Strissel et al., 2005). The translocation of these proteins has been hypothesized to be governed by either IFT (Marszalek et al., 2000) or by diffusion driven by a gradient created by light-dependent changes in local binding (Nair et al., 2005; Calvert et al., 2006). Whether by IFT or by diffusion, the proteins must pass through the CC, i.e., a short segment of the whole photoreceptor sensory cilium that joins the OS and IS compartments, and which preserves the classical ultrastructure of a primary cilium with plasma membrane in close apposition to the axoneme (Fig. 1 D).

The utility of the retinal rod as a preparation for investigating diffusional movement through a primary cilium arises from the relatively large diameter of the rod cell on either side of the much narrower CC, and from two additional felicitous features of the adjoining IS and OS. The large diameter of the rod allows accurate, high resolution confocal measurement of fluorescent protein concentrations on either side of the CC (e.g., Peet et al., 2004). One of the felicitous features of rods is that the cytoplasm of the IS proximate to the CC, the myoid, is relatively unstructured, so that (as data presented here will demonstrate) it very rapidly equilibrates upon sudden, local changes in fluorescent protein concentration. In contrast, on the OS side of the CC the lamellar disc stack, which occupies most of the cross section of the rod, greatly retards the longitudinal diffusion of proteins so that concentration changes in the IS are not rapidly dissipated from the base of the OS after propagating there through the CC. It follows from these features that an experimenter, using appropriate methods of confocal microscopy, can quickly create a change in concentration of a soluble fluorescent protein in the IS, and then, by measuring the gradient of fluorescent protein across the CC and its redistribution between the two segments, estimate its apparent diffusion coefficient within the CC using Fick's first law or its embodiment in the full solution of appropriate diffusion equations.

MATERIALS AND METHODS

Generation of transgenic *Xenopus laevis* expressing photoactivatable green fluorescent protein (PAGFP)

A plasmid containing the coding sequence of PAGFP (Patterson and Lippincott-Schwartz, 2002) was provided by G.H. Patterson and J. Lippincott-Schwartz (National Institutes of Health [NIH], Bethesda, MD). Transgenic *Xenopus laevis* were generated using the REMI method (Kroll and Amaya, 1996). In brief, the coding

sequence of PAGFP was placed downstream from the *Xenopus* opsin promoter, which confined expression specifically to the rod photoreceptors (Mani et al., 2001). The plasmid was linearized with XhoI endonuclease and incubated with isolated *Xenopus laevis* sperm nuclei that were similarly digested. Eggs were fertilized by injection of the sperm nuclei. Transgenic embryos were identified by epifluorescent fundus imaging and allowed to develop into tadpoles and adult frogs.

Tissue preparation

Xenopus tadpoles, stage 42–60, expressing PAGFP in rods were dark-adapted for at least 2 h before experiment. All subsequent procedures were performed under infrared illumination to minimize activation of the light receptor, rhodopsin. Tadpoles were anesthetized by bathing in 0.05% tricaine (Ethyl 3-aminobenzoate methanesulfonate; Sigma-Aldrich) and decapitated. Eyes were removed and retinas were dissected into frog Ringer's solution (in mM: 120 NaCl, 2 KCl, 10 HEPES, 1.6 MgCl₂, 10 glucose, 0.03 EDTA, and 1.0 CaCl₂). Retinas were oriented ganglion cell side down in a 50- μ l bubble of Ringer's on a polypropylene sheet and sliced into strips \sim 50–100- μ m wide and 100–200- μ m long. Slices were transferred to an imaging chamber that consisted of a 35-mm polystyrene Petri dish, into the center of which a 5-mm diameter hole was drilled and then covered with a No. 1 glass coverslip attached with tackywax, which formed the bottom of the chamber. A moist sponge was placed in the Petri dish and the lid was loosely applied, such that humidity prevented evaporation of the Ringer's solution while allowing free gas exchange. The chamber was then placed onto the stage of the inverted confocal/multiphoton microscope. All procedures and experiments were performed at 21°C within 2 h of retinal dissection. Experiments were conducted in accordance with the NIH Guide for the Care and Use of Laboratory Animals.

Multiphoton photoconversion of PAGFP and imaging in live *Xenopus* rods

Imaging and protein flux measurements were performed with a custom-built confocal/multiphoton microscope described previously (Peet et al., 2004; Calvert et al., 2007) that was modified by the addition of a custom LabVIEW-based software interface that allows for rapid (up to 12 Hz) image acquisition and protocols that control the laser intensity and positioning for photoconversion of fluorescent molecules (designed and implemented in conjunction with Michael Coleman, Coleman Technologies Inc.).

Transgenic expression of proteins under the *Xenopus* opsin promoter results in heterogeneous protein levels across rods in a given animal's retina (Peet et al., 2004). Thus, 3-D scans of the retinal slices were performed before experiment to identify rods with sufficient PAGFP expression and that were well oriented with their long axis as close to parallel to the x-y image plane as possible. The initial 3-D scans were performed with visible, confocal scanning using the 488-nm line of an argon-ion laser (model 163C; Newport Corp.) focused to the diffraction limit with a 60 \times , 1.2 NA, water-immersion objective (Plan Apo VC; Nikon). The 3-D coordinates for the photoconversion pulse were manually selected from these initial scans using the LabVIEW interface.

PAGFP was photoconverted at the specified coordinates by multiphoton excitation from the Ti:S laser (Mai Tai HP; Newport Corp.) tuned to 820 nm and focused to the diffraction limit. The use of multiphoton excitation allowed the production of spatially well-defined fields of photoconverted molecules (Zipfel et al., 2003) and minimized the exposure of the tissue to visible light. The laser exposures ranged from 0.1 to 100 ms and 10 to 20 mW (average power). The equilibration of the photoconverted PAGFP was then monitored with serial x-y scans with 488-nm confocal excitation that intersected the photoconversion site. Rapid focus

corrections were made before and after the photoconversion pulse to account for the measured focus difference between 820- and 488-nm illumination caused by objective chromatic aberration (Calvert et al., 2007).

Raw images were processed using custom MATLAB (The MathWorks) routines to correct for slight field inhomogeneities inherent to the optical system and for nonlinearities in the photon detectors as follows. Full field scans with each laser in the system of solutions of fluorescein were averaged to generate image field-flattening maps. Except where noted, no other image processing was done.

The 3-D point spread functions (psf) were estimated from spatial fluorescence distribution patterns obtained during 3-D scans of 0.1- μm fluorescent microspheres (Polysciences, Inc.), as described previously (Calvert et al., 2007). The fluorescence profiles in x,y and x,z were approximated by peak normalized Gaussians with $\sigma_{x,y} = 0.16$ and $\sigma_{z1} = \sigma_{z2} = 0.68$ for the focused Ti:sapphire laser tuned to 820 nm (multiphoton excitation, cf. Eq. 6 in Theory section), and $\sigma_{x,y} = 0.16$ and $\sigma_z = 0.61$ for the 488-nm line of the argon ion laser.

Online supplemental material

Although the approaches used to model the diffusional movement of PAGFP in the rod are presented in the Theory section, additional theoretical details of the methods used to obtain numerical solutions to equations, process and fit the data with theoretical curves generated by the model, as well as video clips of PAGFP diffusing in the IS and OS compartments and equilibrating throughout the rod cytoplasm are available at <http://www.jgp.org/cgi/content/full/jgp.200910322/DC1>.

THEORY

In this section, we present three distinct approaches to the use of diffusion theory to characterize the movement of soluble proteins in living photoreceptors or in other elongated cells, such as many neurons that possess distinct, interconnected cytoplasmic compartments containing structural elements of variable densities. First, we present a general 3-D model applicable for determination of diffusivities within relatively homogeneous cytoplasm; this model is applied to the IS compartment. We also present two approaches that reduce the problem of diffusion between interconnected cytoplasmic compartments to 1-D; the application of these approaches depends on the hypothesis of “rapid radial equilibration,” which is examined experimentally. One of these approaches is a direct application of Fick’s first law to movement through the CC, whereas the second involves longitudinal or axial diffusion in and between all the interconnecting compartments and incorporates position-specific diffusivities and cross-sectional areas. The overall modeling incorporates two additional important features. The first is the description of the source of photoconverted GFP created by the Ti:sapphire laser, specified in terms of the measured multiphoton point-spread function. The second is a description of the analysis by which the confocal measurement of fluorescence intensity is transformed into local concentration (as required by the diffusion models) in cellular compartments with structurally inhomogeneous cytoplasm.

3-D model of PAGFP excitation and diffusional equilibration in the rod cytoplasm

A model describing the dynamic equilibration of proteins along a concentration gradient produced by the photoactivation of PAGFP in the cytoplasm of rods was developed to assess the mobility of molecules within and between rod compartments. We begin with the description of the distribution of PAGFP in the rod before, during, and after photoconversion. The photoconversion of PAGFP is treated as a rapid, irreversible change of state of the molecule from a basal, B , form to a photoconverted, C , form upon multiphoton absorption after illumination with a pulsed Ti:sapphire laser tuned to 820 nm,



The time-dependent concentration distributions of PAGFP in the two forms are represented as $b(x,y,z,t)$, the basal or unconverted form of PAGFP, and $c(x,y,z,t)$, the converted form. (In the presentation that follows it is helpful to have names to distinguish the two forms; thus, we shall refer to them as “basal-PAGFP” and “converted-PAGFP” or the “b-form” and “c-form.”) As will be explained further, these concentrations are referenced to the cytoplasm. With these considerations, the general system of equations governing the photoconversion and diffusion of PAGFP in three dimensions may be written:

$$\frac{\partial b}{\partial t} = D\nabla^2 b - Q_s \quad (2)$$

$$\frac{\partial c}{\partial t} = D\nabla^2 c + Q_s \quad (3)$$

$$\begin{aligned} Q_s &= \alpha_m^* \gamma^* I^m(x,y,z,t)b, & 0 \leq t \leq \Delta T \\ &= 0, & t \geq \Delta T \end{aligned} \quad (4)$$

$$\begin{aligned} b(x,y,z,t) &= b_0, & t \leq 0 \\ c(x,y,z,t) &= 0, & t \leq 0 \end{aligned} \quad (5)$$

where D is the diffusion coefficient of PAGFP, which is assumed to be identical for the basal and photoconverted states of the molecules, ∇^2 is the Laplacian operator, and Q_s is a source term that describes the generation of photoconverted molecules. The source term Q_s embodies the intensity- and time-dependent photoconversion of PAGFP by a Ti:sapphire laser pulse of duration ΔT , where α_m^* is the effective multiphoton absorption cross section of the basal form of PAGFP, γ^* is the quantum efficiency of photoconversion, and $I(x,y,z,t)$ is the photon flux density at spatial coordinate (x,y,z) and time, t . The superscript m is used to generalize the equation to include flux profiles determined by and describing multiphoton absorption (see below). Eq. 5 describes the initial concentration distributions of the two forms of PAGFP.

The distribution of the basal form of PAGFP in the rod

In addition to its role as the substrate creating the source from which the c-form of PAGFP diffuses, the b-form is of importance in several ways for the experiments and theory. First, because it is, albeit weakly, fluorescent with 488-nm excitation, it serves to identify rods with high levels of expression of PAGFP, which are the most suitable for experimentation. Second, on the hypothesis (presented in detail below) that before photoconversion the b-form is in equilibrium with the water space of the cell, measuring its initial 3-D distribution in a rod targeted for photoconversion serves as a critical baseline for monitoring the progress toward equilibrium.

The multiphoton point spread function and PAGFP photoconversion

The Ti:sapphire laser used to photoconvert PAGFP is focused into the sample to the diffraction limit; thus, the spatial profile of the photon flux density, $I(x,y,z)$, may be approximated as the following Gaussian function normalized to the flux density at the laser focus, $I_0 = I(x=0, y=0, z=0)$,

$$\frac{I^m(x,y,z)}{I_0^m} = \frac{1}{(2\pi)^{3/2}\sigma_{xy}^2} \exp\left(-\frac{1}{2}\frac{x^2+y^2}{\sigma_{xy}^2}\right) \times \left\{ \frac{a_{z1}}{\sigma_{z1}} \exp\left(-\frac{1}{2}\frac{z^2}{\sigma_{z1}^2}\right) + \frac{a_{z2}}{\sigma_{z2}} \exp\left(-\frac{1}{2}\frac{z^2}{\sigma_{z2}^2}\right) \right\}, \quad a_z > 0, \quad (6)$$

where σ 's are the standard deviations of the Gaussian profiles in the direction of the indicated axis, and a_z are scaling factors for the sum of two Gaussians used in the z dimension.

The superscript m used in Eqs. 4 and 6 is used to express the fact that the photoconversion of PAGFP, and indeed the measurement of the $I(x,y,z)$ profile, is achieved by multiphoton absorption by fluorescent molecules. Thus, the effective multiphoton excitation profile is a power law function of the photon flux profile (Zipfel et al., 2003), such that the exponent m denotes the number of (infrared) photons that must be nearly simultaneously absorbed for excitation of a fluorescent molecule (cf. Calvert et al., 2007). Thus, we refer to $I^m(x,y,z)$ as the “multiphoton point spread function,” or *mppsf*.

Source intensity rate parameter

In Eq. 4, the product $\alpha_m^* \gamma^* I_0^m$ has the unit s^{-1} and thus may be treated as a composite “source intensity rate” parameter. This parameter is related to the “bleach depth” parameter of FRAP studies, but it is more general and has the distinct advantage in the context of Eqs. 2–4 that the photoconversion pulse does not need to be short relative to the diffusion of the photoconverted species (cf. Calvert et al., 2007).

Coordinate system

The rod OS is approximately a right-circular cylinder, and other portions of the rod have circular symmetry (Fig. 2 B); thus, it is convenient to describe 3-D positional information within the rod in cylindrical coordinates: two orthogonal coordinate axes, a longitudinal or axial (z) and a radial (r), and an angular coordinate, θ , that describes the rotation about z (Fig. 2 B). The spatial coordinate systems in Cartesian and cylindrical coordinates are:

$$\begin{aligned} \bar{r} &= (x, y, z) && \text{(Cartesian coordinates)} \\ \bar{r} &= (r \cos(\theta), r \sin(\theta), z) && \text{(cylindrical coordinates)} \end{aligned}$$

where θ is the azimuthal angle about the z axis and $r = |\bar{r}| = \sqrt{x^2 + y^2}$, with distance specified in μm . The cylindrical coordinate system allows different values of D for molecular diffusion along the two orthogonal axes, allowing for analysis of anisotropic movement. To implement potential difference in these diffusivities, we have included independent radial, D_r , and axial, D_z , variable diffusion coefficients in our analyses (supplemental text).

Note that the z dimension of the *psf* introduced above refers to the optical light propagation axis and is distinct from the z dimension of the cylindrical coordinate system used in analysis of diffusion in the rod. All discussion of the model output refers to the latter cylindrical coordinate system.

Boundary conditions (BCs)

PAGFP cannot cross the plasma membrane; the addition of 0 flux BCs at the plasma membrane is thus required to complete the system of equations:

$$\frac{\partial c(r, z=l, t)}{\partial z} = \frac{\partial c(r, z=L, t)}{\partial z} = \frac{\partial c(r=0, z, t)}{\partial r} = \frac{\partial c(r=r_0, z, t)}{\partial r} = 0. \quad (7)$$

Eq. 7 describes the case in which photoactivation is centered at $r=0$.

Conservation of PAGFP

Eqs. 2–5, when combined with the no-flux BCs, Eq. 7, imply that the total quantity of PAGFP in the cell, which includes both unconverted and photoconverted forms, should remain constant. Moreover, after a photoconversion exposure, given negligible bleaching by the 488-nm scanning beam, the quantity of photoconverted PAGFP should remain constant as it redistributes throughout the cell. Testing for conservation is an important control for system and cell stability.

Numerical solution of the system equations

To solve the system defined by Eqs. 2–7, we used the numerical methods of lines (Schiesser, 1991; Schiesser and

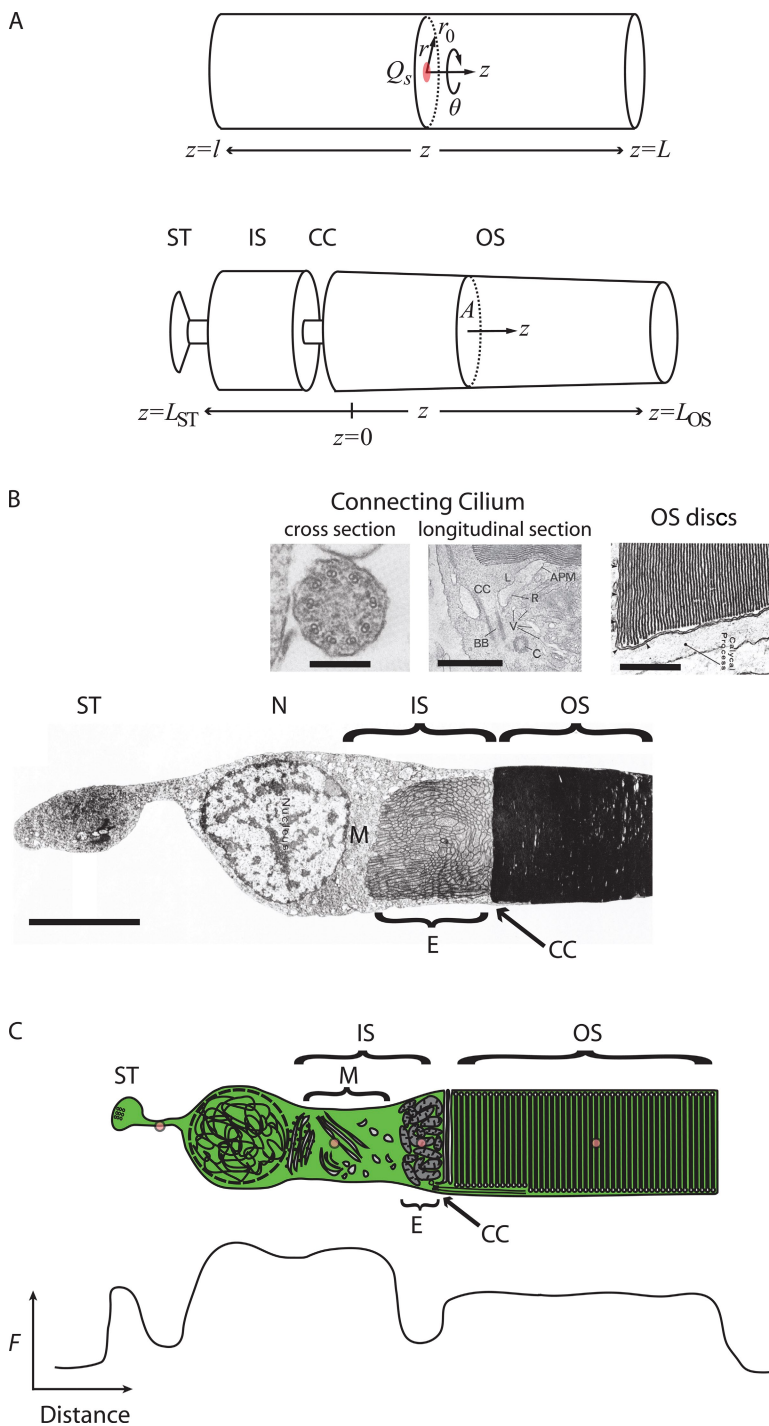


Figure 2. Coordinate systems and structural features of rod photoreceptors important for analyzing molecular motion. (A) Coordinate systems. (Top) The cylindrical coordinate system used in the 3-D model of diffusion in the OS and IS compartments. (Bottom) Coordinates used in the 1-D model of intercompartment diffusion (see Theory). (B) Transmission EM of a rod. A thin section along the central axis of a rod cell isolated from salamander retina showing the axial variation in the density of structures within the major rod compartments. OS, outer segment; IS, inner segment; E, mitochondria-filled ellipsoid; M, myoid; N, nucleus; ST, synaptic terminal; CC, connecting cilium (approximate position). The distal outer segment was truncated in this image. Bar, 10 μm . (CC inset; left) Cross section of a rat rod CC showing the 9 + 0 microtubule motif and the close juxtaposition of the plasma membrane, reproduced from Besharse et al. (1985) with permission. Bar, 0.3 μm . (Right) Longitudinal section of a frog rod CC (reproduced from Peters et al., 1983 with permission). Bar, 1.0 μm . (OS discs inset) Detail showing the stack of membranous discs orthogonal to the axis of the rod. Bar, 1 μm . The isolated rod and the OS disc inset are from Townes-Anderson et al. (1985). (C) Effect of suboptimal resolution structures on fluorescence intensity. The presence of structural inhomogeneities of rods in the volume of the ρ_{psf} result in variation in recorded GFP fluorescence, even when the aqueous concentration (green color) of the protein is uniform. Red circles in the top panel illustrate a cross section of the ρ_{psf} in an x - y image plane of a rod that is occupied to varying degrees by different densities of subcellular structures. The bottom panel illustrates the expected variation in fluorescence (F) (compare Peet et al., 2004).

Griffiths, 2009). In brief, the terms of the Laplacian (∇^2) operator, expressed in cylindrical coordinates, were replaced by appropriate algebraic (finite difference) approximations. The resulting system of ordinary differential equations (ODEs) in time was coded in MATLAB and integrated with a sparse integrator in the MATLAB function library (ode15s). Various tests were used to determine the accuracy of the solutions, including comparison to analytical solutions of special cases of the

model (supplemental text). To compare the model output to fluorescence data, the blurring of the distribution of fluorescent molecules in the cell caused by the scanning ρ_{psf} was accounted for by convolving the model output with a kernel based on the measured ρ_{psf} (Materials and methods). This allowed the estimation of diffusion coefficients within relatively homogeneous cell compartments large enough to accommodate the “volume” of the ρ_{psf} .

Diffusion in the CC: alternative approaches

Some specific problems arise in the application of the general model (Eqs. 2–7) to the CC per se. First, the dimensions of the CC are below the resolution limit of the confocal microscope. Second, the CC presents a discontinuity in the cell radius r_0 between the IS and OS compartments that is difficult to accommodate in the full 3-D model. To circumvent these problems, we used two alternative theoretical approaches. These approaches rest on the assumption that PAGFP molecules equilibrate in the radial dimension of the rod much more quickly than in the longitudinal, thus reducing the problem to a single spatial dimension, the rod axis. This assumption is reasonable for small molecules in the OS of rods (Lamb et al., 1981; Olson and Pugh, 1993) and, as will be shown in Results, can be experimentally justified for PAGFP diffusion in the IS and OS compartments.

Approach 1: Fick's law

The diffusivity of PAGFP in the CC can in principle be estimated with a straightforward application of Fick's first law:

$$\text{flux}_{\text{CC}}(t) = D_{\text{CC}} A_{\text{CC}} \frac{[c_{\text{IS}}(t) - c_{\text{OS}}(t)]}{L_{\text{CC}}} \quad (9)$$

In this expression, $\text{flux}_{\text{CC}}(t)$ is the net flux of the c-form of PAGFP into the OS through the CC at time t after a photoconversion exposure in the IS, $c_{\text{IS}}(t)$ and $c_{\text{OS}}(t)$ are the concentrations of the protein in the IS and OS, respectively, at the locations adjacent to the CC, L_{CC} is the length and A_{CC} the cross-sectional area of the cilium patent to diffusion, and D_{CC} is the diffusion coefficient. To apply Eq. 9, the concentrations $c_{\text{IS}}(t)$ and $c_{\text{OS}}(t)$, as will be shown below, can be extracted with Eq. 20, and the parameters L_{CC} and A_{CC} are estimated from electron micrographs (Table I). The net flux into the OS can be estimated from the total mass of the c-form in the OS; thus, if $M_{\text{OS}}(t)$ is the total mass of the c-form in the OS at time t , estimated from the spatially integrated fluorescence, then $\text{flux}_{\text{CC}}(t) = dM_{\text{OS}}(t)/dt$. Thus, we have the following relation from which D_{CC} can be estimated:

$$\frac{dM_{\text{OS}} / dt}{[c_{\text{IS}}(t) - c_{\text{OS}}(t)]} = \text{const} \quad (10)$$

$$= \frac{D_{\text{CC}} A_{\text{CC}}}{L_{\text{CC}}}.$$

An important feature of Eq. 10 is that it predicts that the ratio of two measurable time-varying quantities should be a time-independent constant.

Approach 2: 1-D model of the rod

The assumption of rapid radial diffusion allows the photoreceptor to be modeled in one spatial dimension,

TABLE I
Dimensions of *Xenopus* rod connecting cilia from EM^a, μm
(mean \pm SD; $n = 6$)

Parameter	Value
Length ^b	0.88 ± 0.10
Diameter IS ^c	0.35 ± 0.06
Diameter OS ^d	0.47 ± 0.12

Difference in proximal and distal diameters not significant at the $P = 0.05$ level ($P = 0.070$).

^aDimensions are based upon published and unpublished EM data (Besharse, J.C., personal communication).

^bLength is measured from the basal body to the first OS disk.

^cDiameter of the IS end measured at the basal body to axoneme transition.

^dDiameter of the OS end measured at the point where the first bulge representing a new disk emerges.

with appropriate accommodations for the variable cross-sectional area (Fig. 2, A and B). Thus, Fick's first law of diffusion in one spatial dimension may be expressed as follows (cf. Crank, 1975):

$$f/A = -D \frac{\partial c}{\partial z}, \quad (11)$$

where f is the flux of molecules (number of molecules per unit time, t) passing through a cross section of area A and, $\partial c / \partial z$ is the gradient of the diffusing species along the axial (z) coordinate. Consideration of mass balance then allows one to write the rate of change of concentration in any volume element along z as the spatial derivative of Eq. 11,

$$\frac{\partial c}{\partial t} = -\frac{\partial (f/A)}{\partial z}. \quad (12)$$

Rearrangement and substitution readily yield Fick's second law of diffusion in one spatial dimension for the case in which both the cross-sectional area and diffusion coefficient are dependent on the axial position (see supplemental text):

$$\frac{\partial c}{\partial t} = \frac{1}{A(z)} \frac{\partial \left(A(z) \cdot D(z) \cdot \frac{\partial c}{\partial z} \right)}{\partial z}. \quad (13)$$

Solution of Eq. 13 allows the time course of equilibration of a diffusing molecular species in the rod to be calculated, given experimental determinations of $A(z)$, $D(z)$, and $\partial c / \partial z$.

Initial and BCs

The natural physical BCs for the problem are “0 flux” at the rod synaptic terminal and at the tip of the OS (Fig. 2 B). However, because the OS and IS differ radically in their

material density and structure, and because the IS equilibrates far more rapidly than the OS, it is convenient and warranted to impose a “pseudo boundary” at a z position (identified as $z = 0$) of our choosing. $c(z = 0, t)$ may be derived from the measured fluorescence intensity at $z = 0$ and used as a time-varying Dirichlet BC. These BCs are implemented as follows:

$$\frac{\partial c(z = L, t)}{\partial z} = 0 \quad (14a)$$

$$c(z = 0, t) = f(t) \quad (14b)$$

Eq. 14a states that there is no flux at either end of the cell, i.e., the synaptic terminal (L_{ST}) or the tip of the OS (L_{OS}) of the rod, whereas Eq. 14b is the Dirichlet BC that states that the concentration at the specific axial position $z = 0$ is a known function of time, $f(t)$.

As initial condition, the model assumes PAGFP to be completely equilibrated before the application of the photoconversion exposure and there to be none of the photoconverted form:

$$\begin{aligned} b(z, t = 0) &= b_0 \text{ for all } z, \text{ and} \\ c(z, t = 0) &= c_0 = 0. \end{aligned} \quad (15)$$

Evidence supporting this assumption will be presented.

Solutions

Eqs. 13–15 were solved by means of the numerical method of lines (Schiesser, 1991; Schiesser and Griffiths, 2009). Further explanation of the BCs and details of the method of solution are presented in the supplemental text.

The relationship between measured fluorescence and PAGFP concentration

The application of alternative approaches 1 or 2 to measure the diffusion of PAGFP through the CC requires determination of the concentration gradient between the IS and OS compartments (Eqs. 10 and 13). The simplest approach to estimating the gradient would be to assume that the concentration of converted-PAGFP is everywhere proportional to the specific fluorescence attributable to that form of protein, with the same proportionality constant. This assumption is reasonable for cells such as Chinese hamster ovary (CHO) cells, whose cytosol is largely homogeneous (Calvert et al., 2007) but clearly invalid for rods (Fig. 2, B and C). Thus, the rod interior is to varying degrees occupied by organelles such as mitochondria in the IS or structural elements such as the discs of the OS, which exclude PAGFP. When the psf exceeds the size of such structures, a spatially varying fluorescence distribution is expected, even if

PAGFP is present at the same concentration throughout the cytosol (Fig. 2 C) (Peet et al., 2004).

The enhanced green fluorescent protein (EGFP)/PAGFP equilibration hypothesis

In a previous paper (Peet et al., 2004), we proposed and found support for a hypothesis about EGFP that provides a basis for resolving the problem of inferring concentrations from fluorescence in the presence of subcellular structures or organelles that cannot be resolved with confocal/multiphoton microscopy. The hypothesis proposes that EGFP equilibrates with the communicating water spaces of cells, such that at equilibrium each volume element of the cell contains a quantity of EGFP proportional to its accessible water space. Because PAGFP diffuses both in aqueous solutions and in live CHO cells with diffusion coefficients identical to those of EGFP (Calvert et al., 2007), it is reasonable to hypothesize that both the b-form and c-form of PAGFP equilibrate with the cytoplasm in the same manner as EGFP; therefore, here we generalize the name of the hypothesis to the “EGFP/PAGFP equilibration hypothesis.”

The specific fluorescence F recorded for 488-nm excitation when the psf is centered at a location (x_0, y_0, z_0) is the convolution of the psf and the concentrations of the two forms of the PAGFP:

$$\begin{aligned} F(x_0, y_0, z_0) &= K \iiint I(x - x_0, y - y_0, z - z_0) [\alpha_b \gamma_b b(x, y, z) + \alpha_c \gamma_c c(x, y, z)] dx dy dz \\ &= K I_0 \iiint psf(x - x_0, y - y_0, z - z_0) [\alpha_b \gamma_b b(x, y, z) + \alpha_c \gamma_c c(x, y, z)] dx dy dz \end{aligned} \quad (16)$$

In Eq. 16, K is a system constant that embodies the collection efficiency of the objective, and the optical transmission and capture of fluorescence emission by the system detectors, α_b and α_c are the effective molecular cross sections of the fluorescent species at the excitation wavelength, γ_b and γ_c are the quantum efficiencies of fluorescence given absorption, and $b(x, y, z)$ and $c(x, y, z)$ are the concentrations of the b-form and c-form of PAGFP in the elemental volume $dx dy dz$, understood to be a very small fraction of the psf volume. The second line of Eq. 16 restates the first in terms of the psf , where $psf(x, y, z) \equiv I(x, y, z) / I_0$ and I_0 is the photon flux density at the center of the psf .

The efficiency $\alpha_b \gamma_b$ of exciting fluorescence from basal-PAGFP with 488-nm illumination is $\sim 1\%$ that of the photoconverted state, $\alpha_c \gamma_c$ (Patterson and Lippincott-Schwartz, 2002). Nonetheless, the initial distribution $b(x, y, z)$ of the b-form can be measured, provided care is taken to exclude autofluorescence artifacts (Calvert et al., 2007). Before a photoconverting exposure, $c(x, y, z)$ in Eq. 16 is 0, and in post-processing scan data, the fluorescence

attributable to the initial distribution $b(x,y,z)$ can be subtracted voxel by voxel to extract $c(x,y,z,t)$.

The EGFP/PAGFP equilibration hypothesis can be expressed in the terms of Eq. 16. Initially, before photoconversion, when only the b-form of PAGFP is present in the cell and equilibrated in the cytoplasm, the hypothesis is expressed as

(17)

$$\begin{aligned} & F_0(x_0, y_0, z_0) \\ & \equiv K \alpha_b \gamma_b \iiint I(x - x_0, y - y_0, z - z_0) b_0(x, y, z) dx dy dz \\ & = K \alpha_b \gamma_b b_{aq,0} I_0 \iiint psf(x - x_0, y - y_0, z - z_0) f_{aq}(x, y, z) dx dy dz, \end{aligned}$$

whereas after a photoconversion exposure when the cell has again equilibrated, the hypothesis applied to the combined fluorescence from the b-form and c-form is

(18)

$$\begin{aligned} & F_\infty(x_0, y_0, z_0) \\ & \equiv K \iiint I(x - x_0, y - y_0, z - z_0) (\alpha_b \gamma_b b_\infty(x, y, z) + \alpha_c \gamma_c c_\infty(x, y, z)) dx dy dz \\ & = K (\alpha_b \gamma_b b_{aq,\infty} + \alpha_c \gamma_c c_{aq,\infty}) I_0 \iiint psf(x - x_0, y - y_0, z - z_0) f_{aq}(x, y, z) dx dy dz. \end{aligned}$$

In Eqs. 17 and 18, the subscripts "0" and "∞" represent the initial equilibrated prephotoconverted state and the final post-photoconverted state after reequilibration, respectively, and f_{aq} is the aqueous fraction of the volume element. The "≡" signs in the first lines of Eqs. 17 and 18 indicate that the expression is definitional, whereas the second line embodies the equilibration hypothesis. Thus, in Eq. 17, $b_{aq,0}$ represents the initially equilibrated concentration of the b-form of PAGFP, whereas in Eq. 18, $b_{aq,\infty}$ and $c_{aq,\infty}$ are the finally equilibrated concentrations of the two forms in a volume element of pure cytosol, and $b_\infty(x, y, z)$, $c_\infty(x, y, z)$ are the equilibrated concentrations in a partially obstructed volume element. It follows from Eq. 18 that in an equilibrated cell, the fractional water space at location (x_0, y_0, z_0) can be estimated as

$$\begin{aligned} \bar{f}_{aq}(x_0, y_0, z_0) & \equiv F_\infty(x_0, y_0, z_0) / F_{\max,\infty} \\ & = \frac{\iiint psf(x - x_0, y - y_0, z - z_0) f_{aq}(x, y, z) dx dy dz}{\iiint psf(x - x_0, y - y_0, z - z_0) dx dy dz} \end{aligned} \quad (19)$$

(cf. Peet et al., 2004); in the denominator of Eq. 19, f_{aq} is presumed to be unity, that is, maximal fluorescence is obtained from volume elements that are "pure cytosol." Thus, \bar{f}_{aq} is a volumetrically weighted average estimate of $f_{aq}(x, y, z)$, with the psf acting as the 3-D weighting function.

Consider now a time t after a photoconversion exposure, and let $\Delta F(x, y, z, t)$ be the incremental fluorescence,

i.e., the measured fluorescence with the preexposure fluorescence due to the basal form of PAGFP subtracted. Then, the concentration of the c-form of the fluorescent protein in the cytosolic component of a volume element can be estimated as

$$\bar{c}(x, y, z, t) = \frac{\Delta F(x, y, z, t)}{I_0 K \bar{f}_{aq}(x, y, z) \alpha_c \gamma_c (1 - \delta)}, \quad (20)$$

where $\delta = \alpha_b \gamma_b / \alpha_c \gamma_c \approx 0.01$ and the psf volume is normalized. Two caveats for the application need to be mentioned. First, the volume of the psf sets the scale of relevant structural inhomogeneities. Second, there is no a priori guarantee that there exists in the cell a cytosolic volume the size of the psf that is not to some degree obstructed.

Prediction of uniform scaling of fluorescence after photoconversion

Because the application of the diffusion model rests on the validity of the EGFP/PAGFP equilibration hypothesis via Eq. 20, it is worthwhile to make and test quantitative predictions of the hypothesis that do not depend on the model. The first such prediction follows readily from Eqs. 17 and 18 and relates the distribution of fluorescence $F_\infty(x, y, z)$ of the equilibrated c-form of PAGFP after a photoconversion exposure, with the initial fluorescence distribution $F_0(x, y, z)$ of the b-form:

$$F_\infty(x, y, z) = u F_0(x, y, z), \quad (21)$$

with $u = [(\alpha_c \gamma_c c_{aq,\infty} + \alpha_b \gamma_b b_{aq,\infty}) / \alpha_b \gamma_b b_{aq,0}]$ a scalar quantity. This relationship follows because all distributions of fluorescence arising from equilibrated PAGFP must be proportional to one another, as they depend only on $f_{aq}(x, y, z)$ and constants of the system and protein. A closely related prediction is that the scale factor u in Eq. 21 can be obtained from the total or spatially integrated fluorescence:

$$F_{\text{tot},\infty} = u F_{\text{tot},0}, \quad (22)$$

where $F_{\text{tot}} = \iiint F(x, y, z) dx dy dz$ is the integrated cell fluorescence. Confirmation of these predictions provides support of the PAGFP equilibration hypothesis, and of the estimation of $\bar{f}_{aq}(x, y, z)$ in the rod before exposure to a photoconversion stimulus, allowing $c(x, y, z, t)$ to be derived from Eq. 20.

RESULTS

Equilibration of photoconverted PAGFP between rod cytoplasmic compartments

Retinal slices were scanned in 3-D at 488 nm to find rod cells that had suitably high PAGFP expression levels and that were well aligned for imaging, i.e., with their longitudinal axis nearly parallel to the imaging plane (Fig. 3 A).

The central-most image plane in the z dimension that contained a suitable cell was then selected as the focal plane (z coordinate) at which to photoconvert and monitor PAGFP over time (Fig. 3 B). The x - y coordi-

nates for PAGFP photoconversion were then manually selected from the image based on spatial cues, such that the photoconversion pulse would be localized to the myoid region of the IS (Fig. 3 B, red dot in the IS region),

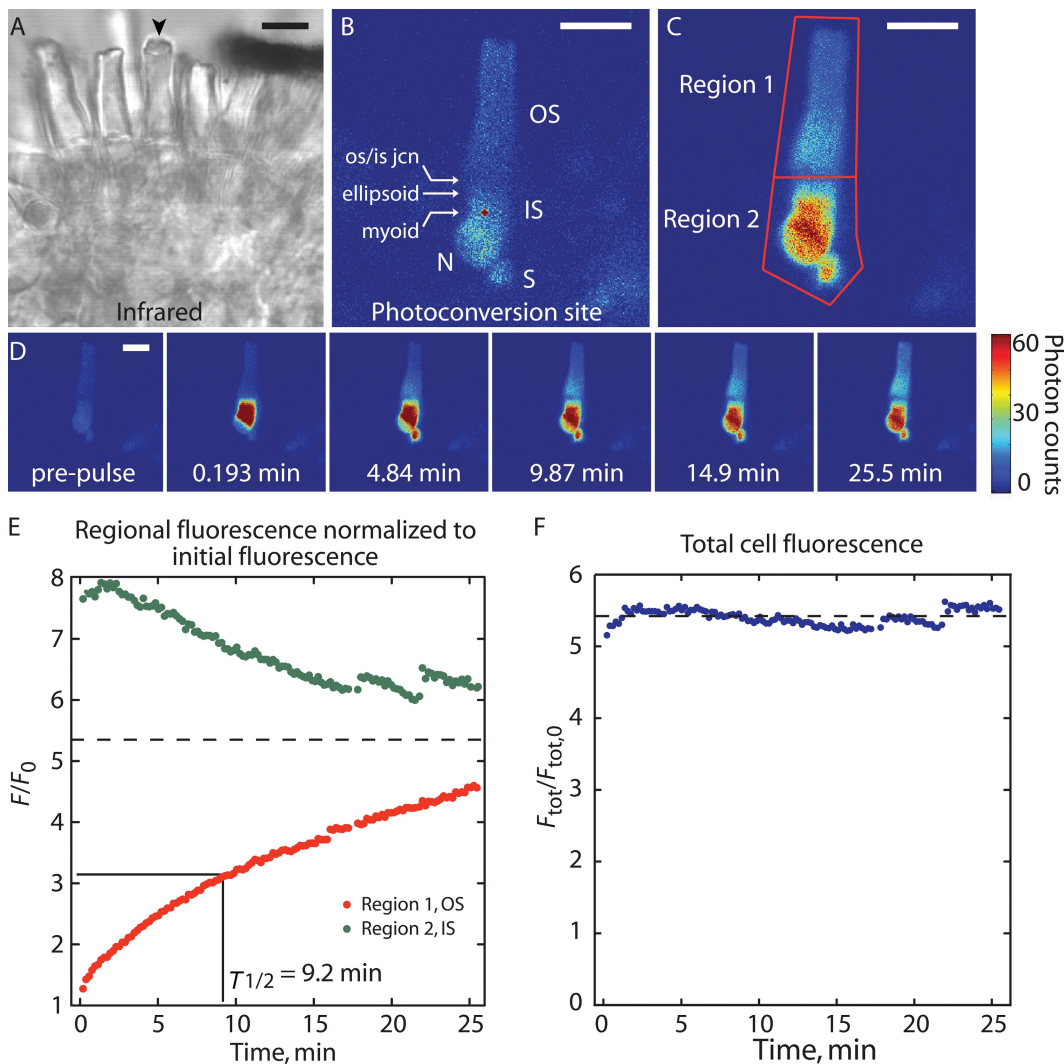


Figure 3. Equilibration of PAGFP throughout the cytoplasm of a rod after photoactivation in the IS. (A) Infrared image of the retinal slice before experiment. The rod in which PAGFP was photoconverted is indicated by the arrowhead. (B–D) All images were obtained with the microscope operating in confocal mode, with the power of the 488-nm argon ion laser line attenuated to 2 μ W (at the sample). (B) Initial fluorescence distribution of PAGFP in the central z image of the rod, intensity scaled to more clearly show the cell structure. The red dot in the center of the image is an overlay of the field intensity profile of the psf , indicating the spatial position in x - y and the dimensions of the multiphoton photoconversion pulse. OS, outer segment; IS, inner segment; N, nucleus; S, synaptic region. (C) The final time series image of the rod (25.5 min from the onset of photoconversion), where the boundary between the IS and OS was more clearly identifiable, was used to delineate regions (red polygons) over which fluorescence levels were integrated in each of the time series images. See results for details of the analysis. (D) Selected images of the fluorescence time series, starting with an image taken just before the photoconversion exposure. Photoconversion was effected by a 100-ms, 20-mW (at the sample) pulse from the Ti:S laser tuned to 820 nm. The times in subsequent images are measured from the moment of pulse initiation. The color bar to the right codes the fluorescence intensity in photon counts and is relevant to the images in C and D only. (E) The integrated fluorescence (F) in the OS (Region 1 in C) and the IS (Region 2 in C), normalized to the integrated fluorescence within the respective region just before photoconversion (F_0), as a function of time after the photoconversion pulse. The dashed line drawn at $F/F_0 = 5.3$ indicates the time-averaged magnitude of total cell fluorescence increase post-photoconversion, and thus represents the value of F/F_0 expected for all compartments upon equilibration (see Fig. 5 and Results for details). $T_{1/2}$ is the time required for the OS compartment to reach 1/2 the F/F_0 value at equilibrium. (F) Integrated fluorescence over the entire cell image normalized to the integrated prepulse fluorescence ($F_{tot}/F_{tot,0}$), as a function of time from pulse onset. The total post-pulse fluorescence remains within ~7% of the median post-pulse value. (A–D) Bars, 10 μ m. See Video 1.

which was identified as the midpoint between the nucleus, the protuberance just distal to the synapse, and the ellipsoid, the region of lower fluorescence just proximal to the OS (Peet et al., 2004). Proper placement of the photoconversion pulse was confirmed after experiment from examination of the pattern of diffusing, photoactivated PAGFP. In a few cases, PAGFP was inadvertently activated in the nucleus, which was evident by rapid nuclear filling. These cells were excluded from the analysis.

Time course of photoactivated PAGFP equilibration

To quantitatively examine the kinetics of photoactivated PAGFP equilibration throughout the entire cytoplasm, the fluorescence changes were evaluated in two subregions of the cell at \sim 10-s intervals, one that encompassed the OS and the other that included the IS photoconversion site, the nucleus, and the synapse (Fig. 3 C; images just before and at several times after the photoconversion exposure are shown in Fig. 3 D; see [Video 1](#)). In this analysis, the final time course image (25.5 min for the cell shown in Fig. 3) was used to delineate the regions of fluorescence to be integrated because the boundary between the OS and the IS compartments was more clearly evident. The integrated fluorescence (F) within the regions in each time course image was normalized to the integrated fluorescence in the respective regions in the pre-photoconversion image (F_0) and plotted as a function of time from the photoconversion pulse onset (Fig. 3 E).

Conservation of photoactivated PAGFP mass

To test mass conservation, the total fluorescence increase in the x,y images taken after the photoactivation pulse (F_{tot}) was normalized to the total fluorescence in the pre-conversion image ($F_{\text{tot},0}$) and examined over the time course of the experiment (Fig. 3 F). Conservation was used as a criterion for cell integrity over the time course of the experiment, and cells failing this test were rejected from further analysis. The total fluorescence in the cell depicted in Fig. 3 increased

5.3 ± 0.10 -fold (mean \pm SD) and varied little (SD $<$ 2% of the time-averaged fluorescence increase), indicating that the mass of photoconverted PAGFP was stable throughout the experiment.

Half-time of PAGFP equilibration between IS and OS

The ratio $F_{\text{tot}}/F_{\text{tot},0}$ provides the expected scaling factor for the fluorescence increase in any local region of the rod upon equilibration of PAGFP after a focal photoconversion exposure (Eqs. 21 and 22). For the rod of Fig. 3, $F_{\text{tot}}/F_{\text{tot},0} = 5.3$ (Fig. 3 E, dashed line). This value was used to estimate the half-time of equilibration of the OS after the photoconversion pulse. For the rod of Fig. 3, the time to 50% equilibration was 9.2 min (Fig. 3 E), and it was \sim 85% equilibrated at 25.5 min. On average, the time to half equilibration was 7.0 ± 1.0 min (Table II). This result is in contrast to the time course of GFP equilibration in mouse rods after photobleaching in rod OSs at room temperature, which was reported to be complete within \sim 3 min ($T_{1/2}, \sim$ 30 s) (Nair et al., 2005). This difference can be explained on the basis of the different sizes of these cells (see Discussion).

PAGFP diffusion between compartments proximal to the OS-IS junction

The diffusion of photoactivated PAGFP between IS compartments was examined by selecting smaller regions of interest (ROIs) within three major IS structures: the myoid, synaptic region, and nucleus (Fig. 4). The synaptic region equilibrated with the myoid relatively rapidly, within \sim 5–10 min. More precisely, the fluorescence in the synaptic region rose to a peak level approximately equal to that in the myoid within \sim 5 min, and then declined in parallel with the fluorescence in the myoid. This indicates that the cytoplasmic spaces of the myoid and the synaptic region are contiguous and relatively unobstructed. In contrast, the movement of PAGFP into the nucleus and OS compartments occurred much more slowly, indicating barriers to diffusion.

TABLE II
Whole cell PAGFP equilibration parameters

Cell	$t_{1/2}$ equilibration min	D_{CC} Flux method $\mu\text{m}^2 \text{s}^{-1}$	D_{CC} 1-D rod model $\mu\text{m}^2 \text{s}^{-1}$	D_{OS} (axial) $\mu\text{m}^2 \text{s}^{-1}$
1	5	4.5	3.3	0.096
2	6.7	2.0	1.3	0.117
3	9.2	4.0	2.5	0.075
4	5.3	1.4	1.3	0.117
5	nd	nd	3.4	0.062
6	5	3.7	nd	0.074
7	11.5	1.0	1.4	0.033
8	9.9	nd	1.6	0.083
9	3.45	nd	2.0	0.050
mean \pm SEM	7.0 ± 1.0	$2.8 \pm 0.5^{\text{a,b}}$	$2.1 \pm 0.3^{\text{a,b}}$	$0.079 \pm 0.009^{\text{b}}$

^aDifference between D_{CC} obtained by flux method and that obtained from the 1-D rod model was not significant ($P = 0.21$).

^bDifferences between D_{CC} measured by either method and D_{OS} were significant at the $P = 0.01$ level.

It has been shown that GFP and its variants enter the nuclei of *Xenopus* photoreceptors (Peterson et al., 2003; Peet et al., 2004). The mechanism for nuclear filling is not understood. Some have posited that GFP and its variants are actively transported to the nucleus. Results shown in Fig. 4 reveal for the first time that the movement of PAGFP across the nuclear membrane is relatively slow, taking \sim 20 min to equilibrate with the neighboring myoid and synapse compartments. Ongoing experiments and analyses are aimed at testing the hypothesis that this slow movement is purely passive. PAGFP transport into the nucleus provides the interesting prospect of using it as a tracer for the regulation of nuclear pore complex permeability and active protein transport across the nuclear membrane in living retinal photoreceptors, studies that are currently underway.

Test of the prediction of uniform scaling of fluorescence after photoconversion

The EGFP/PAGFP equilibration hypothesis (see Theory) predicts that upon equilibration after a photo-

conversion pulse, the fractional change in fluorescence (u) at all locations within the cell (Eq. 21) will be the same as the fractional increase in total cellular fluorescence (Eq. 22). This prediction is borne out as shown in Fig. 5, which compares the fluorescence of PAGFP in the rod depicted in Figs. 3 and 4 at points along a line that intersects each of the cell's major compartments before and 50 min after photoactivation in the cell's myoid. The fluorescence varies considerably along the line in both images. This variation is interpreted to indicate differences in the aqueous fraction in the different compartments (see Theory; Eq. 19). The bottom panel in Fig. 5 B, which plots the fluorescence after internal normalization to the fluorescence of brightest fifth percentile of voxels in each original image, shows that the distribution of fluorescence is essentially the same before and after photoconversion, after sufficient time for equilibration. Moreover, the ratio of the fluorescence of the brightest voxels was \sim 5.3-fold, the same as the mean $F_{\text{tot}}/F_{\text{tot},0}$ in Fig. 3 F. Similar results were obtained with six cells examined in this way.

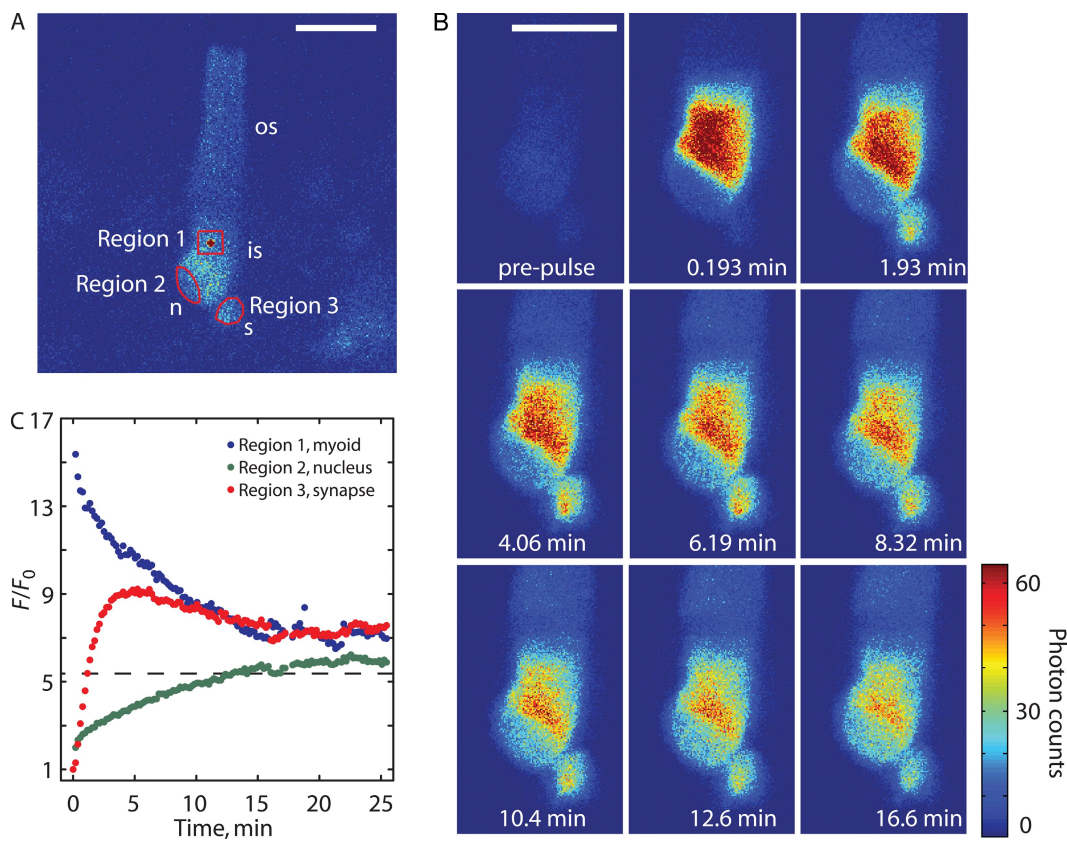


Figure 4. PAGFP diffusion in IS subcompartments. (A) The cell illustrated in Fig. 3 with fluorescence analyzed in the IS subcompartments indicated by red polygons. The red dot shows the site of PAGFP activation. (B) Selected images from the time series in Fig. 3 shown at a higher frequency and enlarged to reveal the dynamics of photoconverted PAGFP in the IS region. The color bar is relevant to images in B only. (C) Integrated fluorescence in each of the regions defined in A, normalized to the integrated fluorescence of the respective regions in the prepulse image. Dashed line indicates the expected equilibrium level (see Fig. 3), which will only be reached when the slowly equilibrating OS is finally at equilibrium. (A and B) Bar, 10 μ m.

Radial equilibration of PAGFP is rapid relative to intercompartmental transport in both the IS and OS. The rates of radial equilibration in the OS and IS compartments (Figs. 6 and 7, respectively) were assessed using a “point blast–ROI scan” protocol (Calvert et al., 2007). Thus, the x,y coordinates for a photoconversion pulse were selected within a confocal scan at the central z plane of a rod cell, such that it would occur at the radial center of the cell. A 2-D ROI centered on the pulse site was then defined (Figs. 6 A and 7 A, green boxes). The ROI was scanned repeatedly before and after a multiphoton photoconversion pulse (Figs. 6 C and 7 C, and Videos 2 and 3). F/F_0 in smaller regions within the acquired ROI (subROIs) near the plasma membrane boundaries were then compared with F/F_0 measured for subROIs that encompassed the photoconversion sites at the radial center of the compartments (Figs. 6 B and 7 B, red boxes). Radial equilibration time was defined as the

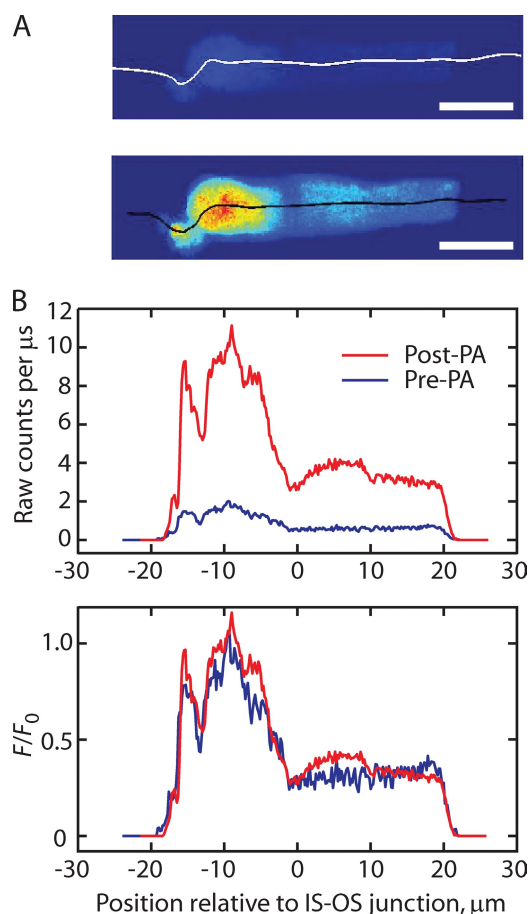


Figure 5. The prediction of uniform scaling of fluorescence after photoconversion holds. (A) Images of the cell from Fig. 3 before and 50 min after the photoconversion (PA) exposure. The lines in the images indicate positions along which fluorescence counts were acquired and compared in B. (B) In the top panel, the raw fluorescence counts along the lines indicated in A are plotted as a function of distance relative to the IS–OS junction. The bottom panel plots the fluorescence normalized to the average of the brightest 5% of the voxels in each 3-D scan (F_0).

time after the photoconversion pulse when the radial F/F_0 values merged with that of the photoconversion site (this definition was used because there is a much slower component of equilibration when OS intercompartmental transport is taken into consideration). The average radial equilibration time in the myoid region of the IS was 2.9 ± 0.6 s ($n = 13$ cells), and in the OS it was 1.9 ± 0.2 s ($n = 12$ cells). These values were not significantly different at the $P = 0.05$ level. Thus, PAGFP equilibrates radially within a few seconds in both the IS and OS compartments, much more quickly than the time required for equilibration between these compartments, which is on the order of tens of minutes (Fig. 3). This result justifies the assumption of rapid radial equilibration in both IS and OS compartments used in the 1-D models applied to measure PAGFP diffusion within the CC.

PAGFP diffusion is isotropic in the myoid and anisotropic in the OS

In addition to radial equilibration, axial equilibration time was assessed. SubROIs were defined at distances equal to those between the photoconversion site ROI and the radial ROIs, but at positions along the orthogonal, axial dimension of the rod (Figs. 6 B and 7 B, axial ROIs). This allowed a direct comparison of the equilibration times in the radial and axial dimensions for a given compartment. In the myoid region, the average axial equilibration time was 3.4 ± 0.8 s ($n = 13$ cells), a value not significantly different from the radial equilibration time at the $P = 0.05$ level. To our knowledge, this is the first assessment of the directional uniformity of molecular diffusion in the IS compartment of rods. In contrast, and not surprisingly, the mean axial equilibration time of 14.5 ± 1.2 s ($n = 12$ cells) in the OS compartment was nearly eightfold slower than that of the radial, presumably due to the highly tortuous axial diffusion path caused by membranous discs in the OS (cf. Fig. 2 B). It should be noted that as defined here, equilibration times are figures of merit and not directly convertible to diffusion coefficients, which must be determined by the application of an appropriate model.

Flux of PAGFP between IS and OS compartments: estimation of the diffusion coefficient in the CC

The flux of PAGFP between the OS and IS compartments was measured according to the direct application of Fick’s first law (Eq. 10 and Fig. 8). Three regions (Fig. 8 A) were selected for analysis in sequential time series images. Region 1, which encompassed the entire OS compartment, defined the area over which OS fluorescence was integrated. Regions 2 and 3, which were chosen within the IS and OS compartments in close proximity to the IS–OS junction, defined regions over which the fluorescence was averaged and to which Eq. 20 was applied to arrive at the water space–corrected relative concentration of protein (Fig. 8 B).

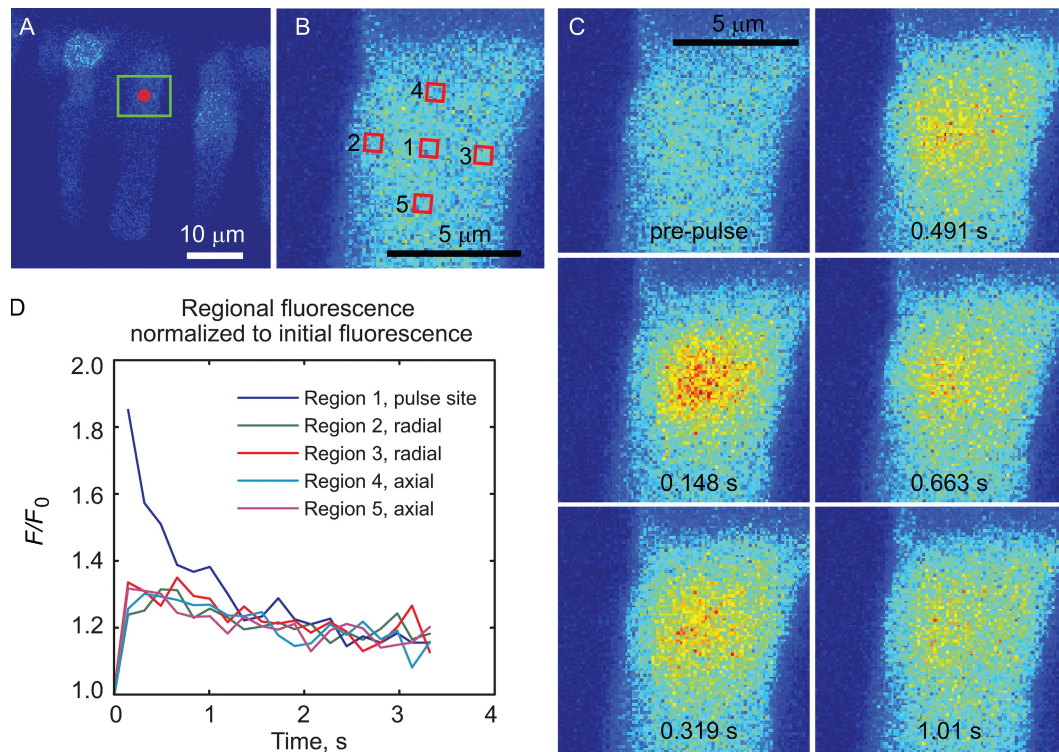


Figure 6. PAGFP equilibration in the myoid is isotropic and rapid. (A) x - y image of the region of retinal slice at the central z level of the cell that was the subject of the experiment. The region of the cell that was rapidly scanned before and after a 100- μ s photoconversion pulse (the location of which is in the myoid, indicated by the red symbol) is delineated by the green box. (B) Pre-conversion scan of the region showing subregions where time courses of fluorescence change were recorded (red boxes). (C) Selected time course images showing the rapid myoid equilibration. (D) Time courses of fluorescence changes recorded from the regions shown in B. Note that the axial and radial regions change in parallel and ultimately merge with the fluorescence time course from region 1, the site of photoconversion, at \sim 1.5 s. See Video 2.

Using the radial symmetry of the OS, the time course of the flux of photoactivated PAGFP into the OS compartment, $dM_{\text{OS}}(t)/dt$, was estimated from the time-dependent change in the mass of activated PAGFP detected in the x , y scan plane, M_{xy} , as follows:

$$\frac{dM_{\text{OS}}(t)}{dt} = \frac{(M_{xy}(t_{i+1}) - M_{xy}(t_i)) \cdot V_{\text{OS}}}{t_{i+1} - t_i}, \quad (23)$$

where $M_{xy}(t) = \iint (F(x, y, t) - F_0(x, y)) \cdot V_{\text{vox}} dx dy$, V_{vox} is the volume of the voxel defined by the x , y spatial sampling frequency, and the psf dimension in z , V_{OS}/V_{xy} is the ratio of total OS envelope volume and the x , y scan plane volume. V_{OS} was determined directly from 3-D scans of the cell as described in the supplemental text. $dM_{\text{OS}}(t)/dt$ and $c_{\text{IS}}(t) - c_{\text{OS}}(t)$ for one cell are shown in Fig. 8 C. Eq. 10 predicts that the ratio $(dM_{\text{OS}}/dt)/[c_{\text{IS}}(t) - c_{\text{OS}}(t)]$ will be constant over time, and this indeed appears to be the case through \sim 6 min after the photoconversion pulse (Fig. 8 D), after which the magnitude of the difference between them becomes too small to accurately measure. The average value of $(dM_{\text{OS}}/dt)/[c_{\text{IS}}(t) - c_{\text{OS}}(t)]$ over the initial 6 min after the photoconversion pulse for the cell depicted was $0.52 \text{ } \mu\text{m}^3 \text{s}^{-1}$. Considering the average

dimensions of the CC (Table I), we obtain an axial diffusion coefficient of PAGFP in the CC of $D_{\text{CC}} = 3.5 \text{ } \mu\text{m}^2 \text{s}^{-1}$. Similar values were obtained from six cells (Table II).

The diffusion coefficient of PAGFP in the myoid region of the IS

The diffusion coefficient D_{IS} in the myoid region of the IS was estimated using the point blast–line scan method (Fig. 9) (cf. Calvert et al., 2007), which provides much higher temporal resolution than the point blast–ROI scan method presented in Figs. 6 and 7. A brief multi-photon photoconversion pulse was applied to the radial center of the myoid, which was followed by rapid (\sim 1-KHz) line scans that intersected the photoconverted PAGFP within the IS cytoplasm (Fig. 9 A, right). The result is a spatiotemporal map of the relaxation of the photoconverted PAGFP within the IS cytoplasm (Fig. 9 A, right). We then applied the 3-D diffusion model described in Theory to the relaxation map varying the diffusion coefficient, D , which was assumed to be uniform for the radial and axial directions (Fig. 9 B). The root mean square difference error between the model and the data was calculated (supplemental text) and plotted as a function of D to arrive at the optimal estimate of D_{IS} for the given cell. On average, $D_{\text{IS}} = 5.16 \pm 0.62 \text{ } \mu\text{m}^2 \text{s}^{-1}$ ($n = 13$ cells).

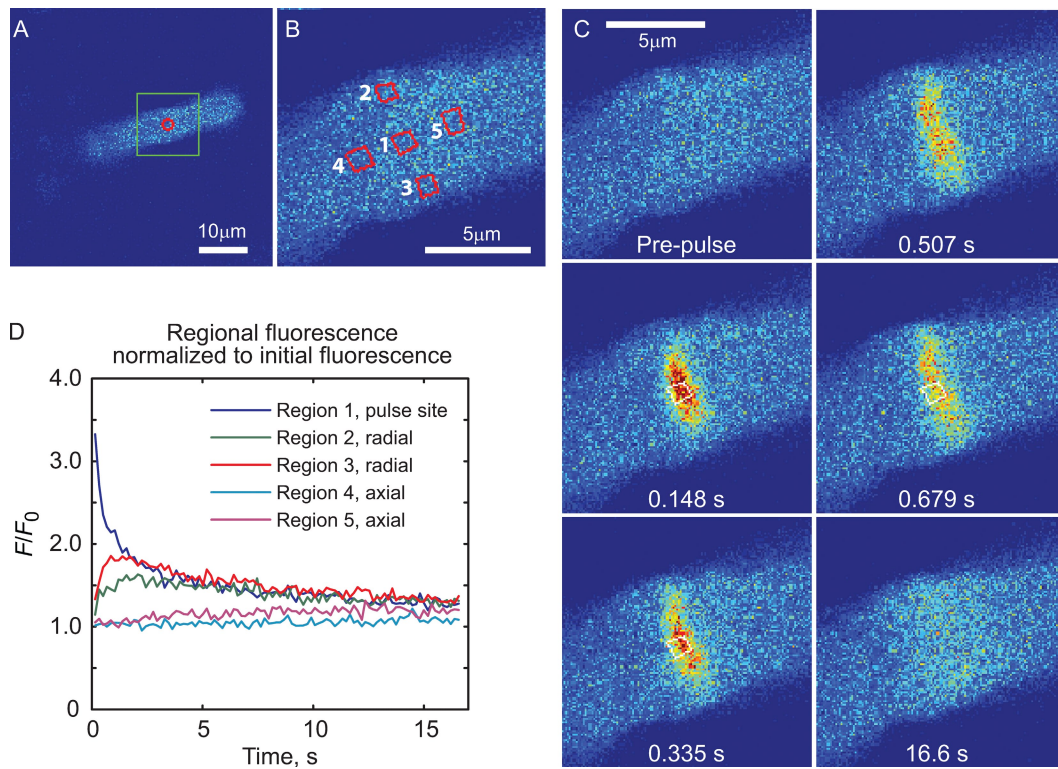


Figure 7. Equilibration of PAGFP in the OS compartment is highly anisotropic. (A) x - y image of the region of retinal slice showing the central z level of the cell at which the experiment was performed. The region of the OS that was rapidly scanned before and after a 100- μ s photoconversion pulse (indicated by the red symbol) is delineated by the green box. (B) Prepulse scan of the region showing subregions where time courses of fluorescence change were recorded (red boxes). (C) Selected time course images showing the rapid radial and slower axial equilibration. (D) Time courses of fluorescence changes recorded from the regions shown in B. Radial positions 2 and 3 changed approximately in parallel and merge with the fluorescence time course from region 1, the site of photoconversion, within \sim 2 s. The fluorescence at axial positions 4 and 5 required much longer, >15 s, to merge with the fluorescence of region 1, demonstrating the high degree of anisotropy in PAGFP diffusion in the OS. See Video 3.

The axial diffusion coefficient of PAGFP in the OS compartment

To estimate the coefficient of diffusion, D_{OS} , of PAGFP along the axial dimension of the OS, the fluorescence levels of voxels within time course images were corrected according to Eq. 20. The corrected fluorescence, $F'(x,z,t)$, was then averaged within a region that was confined to the OS along the radial dimension in each time course image, and $F'(z,t=0)$ was subtracted to arrive at a spatiotemporal map of PAGFP concentration change, $F'(z,t)$ (Fig. 10).

Predicted spatiotemporal maps of PAGFP equilibration, $F'_m(z,t)$, in the OS compartment were then produced from the 1-D diffusion model presented in Theory (Eqs. 13–15). Time-varying Dirichlet BCs in Eq. 14b, $F'_{DB}(t)$, were derived from the averaging of n proximal $F'(z,t)$ values from each of the time course images,

$$F'_{DB}(t) = \sum_{z=1}^n \frac{F'(z(n),t)}{n}, \quad (24)$$

and fitted with a sixth-order polynomial, the result of which was used in model calculations (Fig. 10 B).

The OSs of pre-metamorphic *Xenopus* rods are not generally perfectly cylindrical, instead tapering proximo-distally along the axial dimension of the OS. To account for the tapering in model calculations, the area of cross section as a function of the rod axial position ($A(z)$ in Eq. 13) was determined with a MATLAB routine (see supplemental text). The axial diffusion coefficient in Eq. 13, $D(z)$, was assumed to be constant over all z .

Predicted profiles were thus calculated ($F'_m(z,t)$) (Fig. 10 D) for a range of axial diffusion coefficients and compared with $F'(z,t)$. D_{OS} for PAGFP was determined as the value that produced the smallest E_{RMS} between model prediction and data. For the rod depicted in Fig. 10, $D_{OS} = 0.075 \mu\text{m}^2 \text{s}^{-1}$ produced the model output that best fit the data. D_{OS} values obtained from this and other cells are given in Table II.

Alternative approach to estimating D_{CC}

The 1-D diffusion model with variable cross-sectional area and variable D (Eqs. 13–15) offers an alternative approach to quantifying the diffusion coefficient of PAGFP in the CC. The present analysis is similar to that

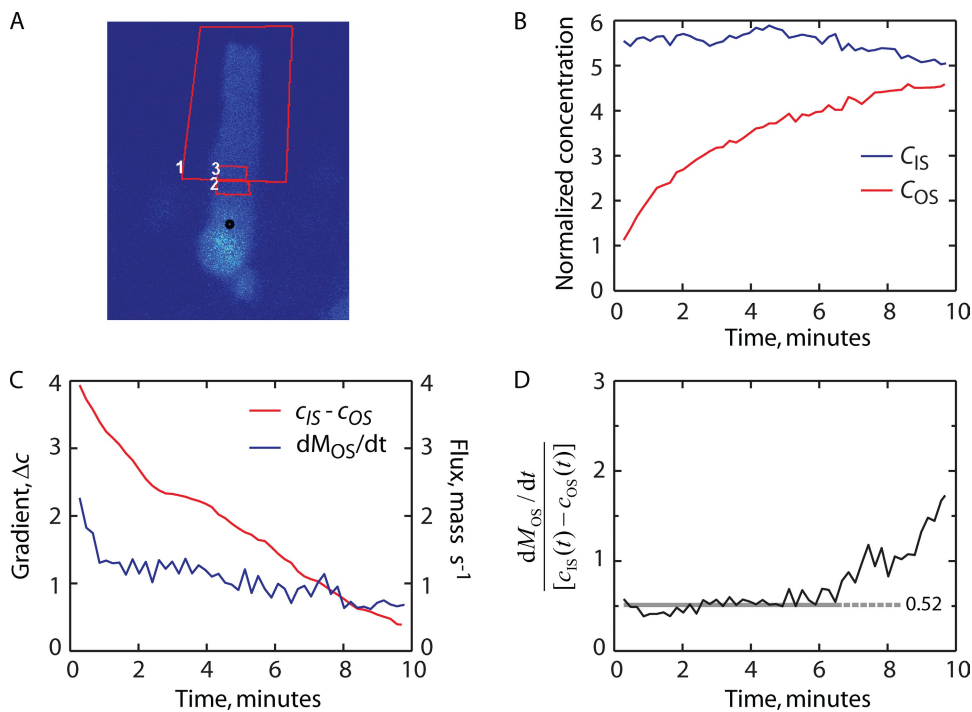


Figure 8. Flux of PAGFP through the CC. (A) Pre-photoconversion image of a rod showing the regions where fluorescence was monitored over time. (B) Relative concentration of photoactivated PAGFP in the IS (region 2) and OS (region 3) after an IS photoconversion pulse. (C) The concentration gradient (red line, left ordinate) and flux (blue line, right ordinate) of PAGFP between IS and OS compartments. (D) The “flux constant” (Eq. 10) as a function of time. Gray line indicates the average value over the first 6.5 min ($0.52 \mu\text{m}^3 \text{s}^{-1}$), after which the $c_{IS} - c_{OS}$ difference fell below $\sim 10\%$ of its original magnitude and became unreliable.

for the axial diffusion of PAGFP in the OS outlined in the previous section, except that the region defined for analysis was extended to include the portion of the cell just proximal to the interface between the IS and OS compartments, thus including the length of rod containing the CC (Fig. 11 A). The predicted $F'_m(z, t)$ was then calculated with diffusion coefficients that varied along the axial dimension of the rod. Three zones of differing diffusion coefficients used in the model, $D_M(z)$, were defined as follows:

$$\begin{aligned} D_M(z) &= D_{IS}, & z < z(CC_l) \\ D_M(z) &= D_{CC}, & z(CC_l) \leq z \leq z(CC_L) \\ D_M(z) &= D_{OS}, & z > z(CC_L), \end{aligned} \quad (25)$$

where D_{IS} is the diffusion coefficient of PAGFP in the IS, the average value determined from point blast-line scan experiments in the IS described in Fig. 9 was used, D_{CC} is the axial diffusion coefficient of PAGFP in the CC, D_{OS} is the diffusion coefficient of PAGFP in the OS determined for the specific cell under investigation as shown in Fig. 10, and $z(CC_l)$ and $z(CC_L)$ are the axial boundaries of the CC. $F_m(z, t)$ was calculated for a range of D_{CC} , and the best value of D_{CC} was considered to be that which produced the minimum value of E_{RMS} . $D_{CC} = 2.5 \mu\text{m}^2 \text{s}^{-1}$ provided the best fit for the rod depicted in Fig. 11. Values for D_{CC} from this and other cells using this method are presented in Table II.

Summary: reduction of diffusion in the rod’s compartments
A useful summary of the results can be made by comparing the effective diffusion coefficients estimated for

PAGFP in the different rod compartments with that measured in aqueous solution and in the relatively unstructured, passed CHO cells. A useful metric capturing the comparison is the “fold-reduction” of the effective diffusion coefficient D_{eff} from that in aqueous solution: (D_{aq}/D_{eff}) (Table III).

DISCUSSION

Quantitative characterization of the steady-state distributions, concentrations, and movements of soluble proteins in living cells is a goal of broad importance for understanding many cellular functions, including cell signaling kinetics and protein renewal mechanisms. Complex polarized cells such as sensory receptors pose many problems to achieving such characterization, for their subcellular “compartments” are differentiated ultrastructurally and often connected by or terminated in narrow constricted structures, such as cilia or axons, whose diameter is near or below the resolution of light microscopy (Figs. 1 and 2). Using the *Xenopus* rod photoreceptor as a model system and PAGFP as a reporter, we have shown how many of the problems can be addressed and in particular have, for the first time, measured the diffusion coefficient of a protein in a primary cilium, as well as in the other major compartments of a highly polarized cell, and also the overall time for the protein concentration to equilibrate within and between compartments.

The CC poses a modest barrier to protein diffusion

The basal body–axoneme complex has been compared with the nuclear pore complex in terms of regulating

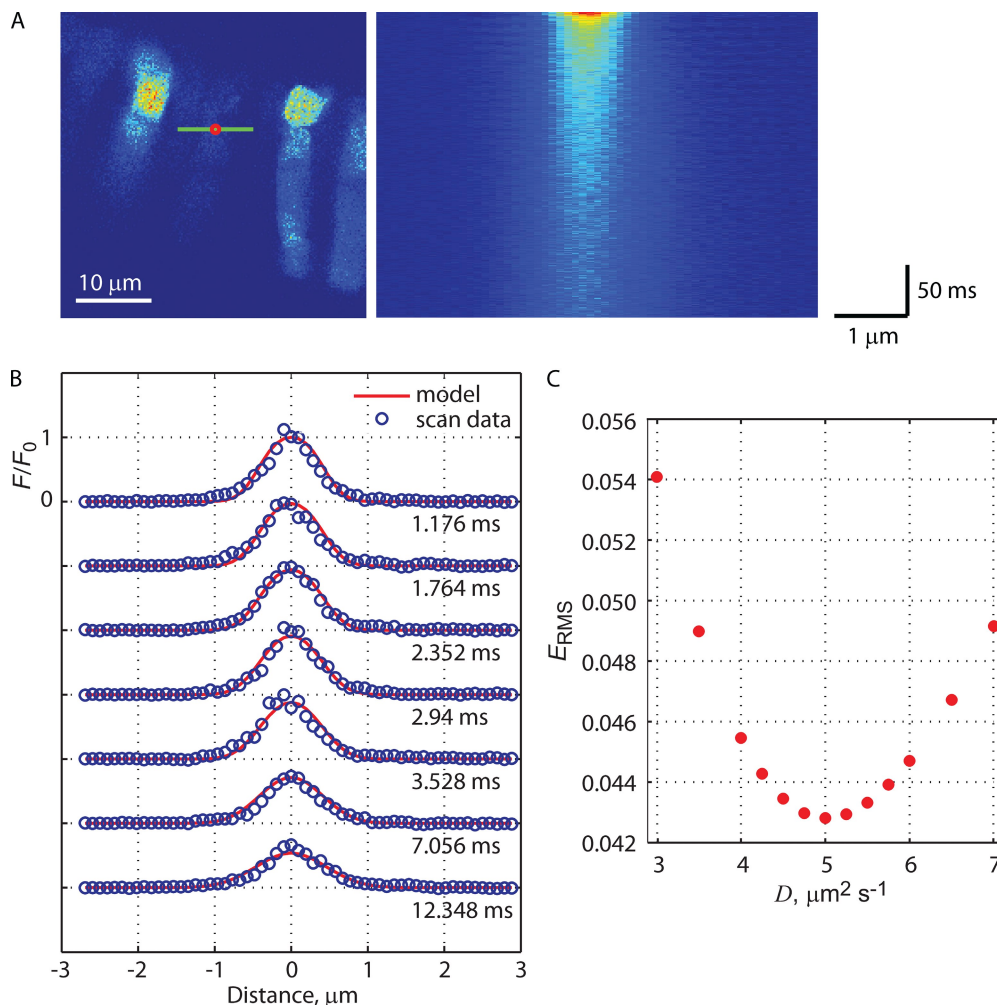


Figure 9. Estimation of the diffusion coefficient of PAGFP in the myoid. (A; left) x - y image of the region of retinal slice showing the z level of the cell on which the experiment was performed. The region of the myoid that was exposed to a 100- μ s photoconversion pulse is indicated by the red symbol. The green line indicates the location of 2-KHz line scans that intersected the photoconversion site. (Right) The spatiotemporal fluorescence map of the dissipation of the photoconverted PAGFP from the photoconversion site. (B) Fluorescence profiles of selected line scans after normalizing to the amplitude of the first post-pulse line scan recorded (1.176 ms). The red lines are the result of model calculations with optimal D . (C) Root mean square (RMS) error calculated from the difference between line scan fluorescence and model prediction for indicated D . Minimal E_{RMS} was achieved with $D = 5 \mu\text{m}^2 \text{s}^{-1}$.

protein access to the cilium (Deane et al., 2001), and it has been proposed that the permeability of the basal body–axoneme complex to protein transport may be regulated in a signal-dependent manner (Wolfrum et al., 2002). The 36-fold reduction in the effective diffusion coefficient of PAGFP in the CC relative to aqueous solution (Table III) provides the first direct evidence that these structures do indeed impede soluble protein movement between the cell body and the cilium, and leaves open the possibility of signal-dependent control of cilium permeability. However, because D_{CC} is only twofold smaller than D_{IS} (Table III) and PAGFP diffusion is more rapid in the IS than anywhere else in the cell, it is difficult to posit that the CC constitutes a highly distinctive barrier to protein movement.

The most distinctive feature of the CC seen in electron micrographs that would be expected to impact protein movement is the 9 + 0 microtubule axoneme and associated structures, but the core of the axoneme appears to offer an unobstructed path for diffusion (cf. Fig. 2). Although the axonemal components will reduce the effective cross-sectional area available for diffusion, as the maximal diameter of each microtubule

doublet is $\sim 37 \pm 1$ nm (Rosenkranz, 1977), the entire axonemal structure reduces the effective cross-sectional area by only $\sim 7\%$, not nearly enough to account for the 36-fold reduction from D_{aq} . It remains possible that the cross-sectional area of the CC available for diffusion of PAGFP is much smaller than apparent from transmission electron micrographs (EMs). Electron tomographic examination of the centrosomal region of chondrocyte cilia (Jensen et al., 2004) shows it to be

TABLE III
Magnitude of reduction of D_{aq} , PAGFP within rod compartments

Cell/compartment	D_{eff}	$D_{\text{aq}}/D_{\text{eff}}$ ratio
$\mu\text{m}^2 \text{s}^{-1}$		
CHO cell cytoplasm ^a	20	4.5
CC	2.5	36
IS	5.2	17
OS	0.08	1,125

The aqueous diffusion coefficient of EGFP, $D_{\text{aq}, \text{EGFP}}$, was reported previously to be 87 (Swaminathan et al., 1997; Brown et al., 1999; Potma et al., 2001) and $91 \mu\text{m}^2 \text{s}^{-1}$ (Calvert et al., 2007). $D_{\text{aq}, \text{PAGFP}}$ was reported to be $89 \mu\text{m}^2 \text{s}^{-1}$ (Calvert et al., 2007).

^aCalvert et al. (2007).

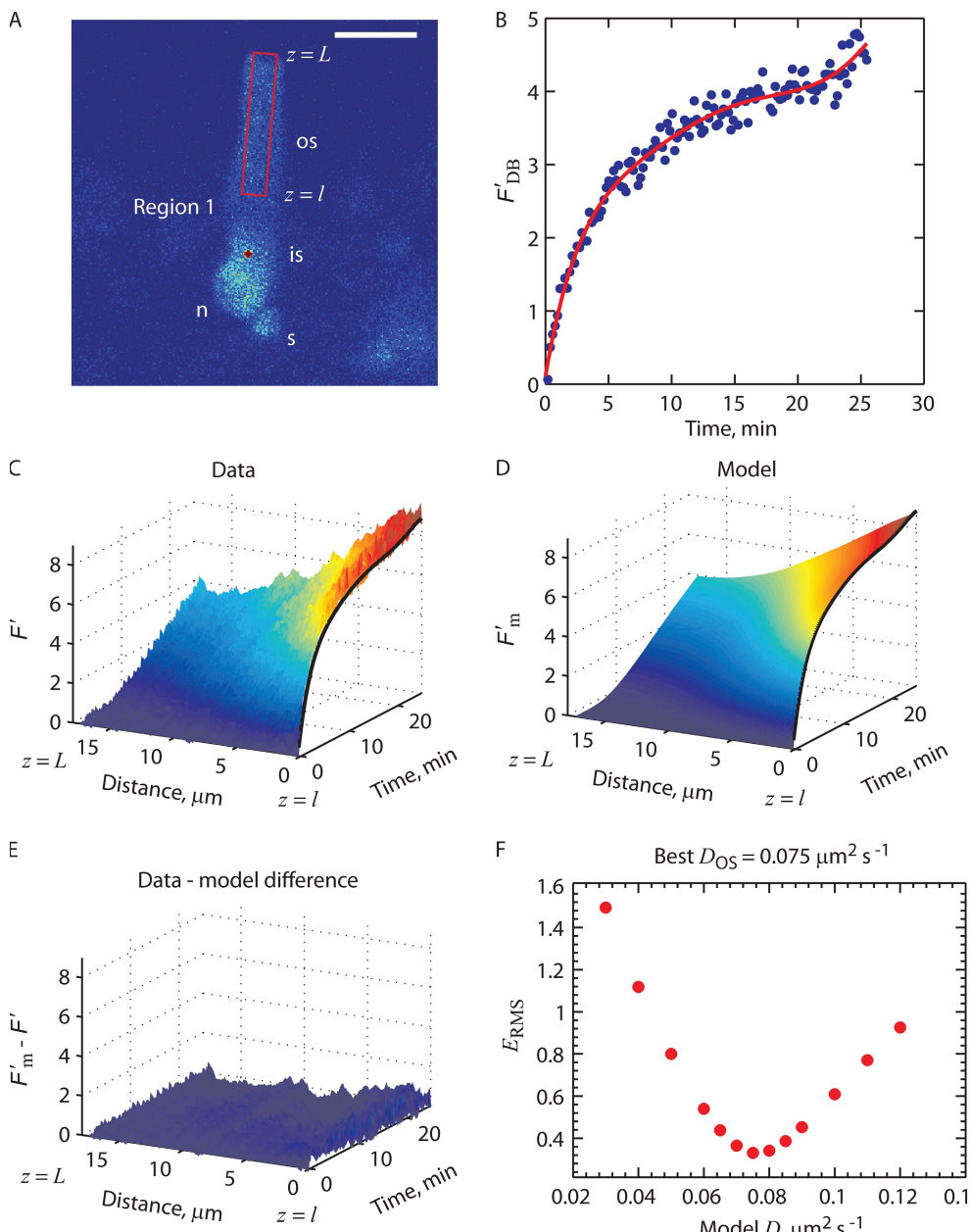


Figure 10. Estimation of the axial diffusion coefficient of PAGFP in the OS compartment. (A) The spatiotemporal profile of activated PAGFP filling of the OS was obtained from the region bounded by the red box. (B) The Dirichlet BC used in calculations was defined by fitting $F'_{\text{DB}}(t)$ for $n = 5$ pixels in z (filled circles) with a sixth-order polynomial (red line). (C) The spatiotemporal profile of activated PAGFP. (D) Eqs. 13–15 were solved with varying D to find the best approximation of the spatiotemporal profile in C. Shown is the model profile, $F'_m(z, t)$, obtained from the solution of best fit. The thick black lines in C and D represent the Dirichlet boundary. (E) The data profile was subtracted from the model profile obtained for each value of D_{OS} to determine the difference error. Shown is the difference for $D = 0.075 \mu\text{m}^2 \text{s}^{-1}$. (F) RMS error values plotted as a function of D .

crowded with fine filamentous material, transitional fibers, and vesicles. Moreover, the lumen of the basal bodies contains large vesicles and electron-dense “plugs” that may occlude or substantially reduce the cross-sectional area available for diffusion. However, as we now discuss, retarded diffusion elsewhere in the rod suggests that more general principles of differentiated cells are at play.

Protein diffusion in the IS is substantially retarded

The IS comprises the region of the rod between the ellipsoid and the nucleus. This region contains the major protein- and lipid-synthesizing and -degrading machinery of the rod and is expected to be homologous to similar regions in most cell types. Diffusion

in the IS of PAGFP is isotropic (Fig. 9) and faster than in any other region of the rod ($D_{\text{IS}} = 5.2 \mu\text{m}^2 \text{s}^{-1}$). Nonetheless, PAGFP diffusion is substantially retarded in the IS, being 18-fold lower than in aqueous solution and fourfold below that in CHO cells (Table III).

Axial diffusion of PAGFP in the OS is retarded 50-fold more than predicted by geometry

The effective coefficient for axial diffusion of PAGFP in the OS, D_{OS} , is reduced 1,125-fold from that in aqueous solution (Table III). The OS comprises densely stacked discs, paired membrane bilayers spaced at $\sim 30 \text{ nm}$, which greatly reduce the patent cross-sectional area, so that most paths for axial diffusion are highly tortuous

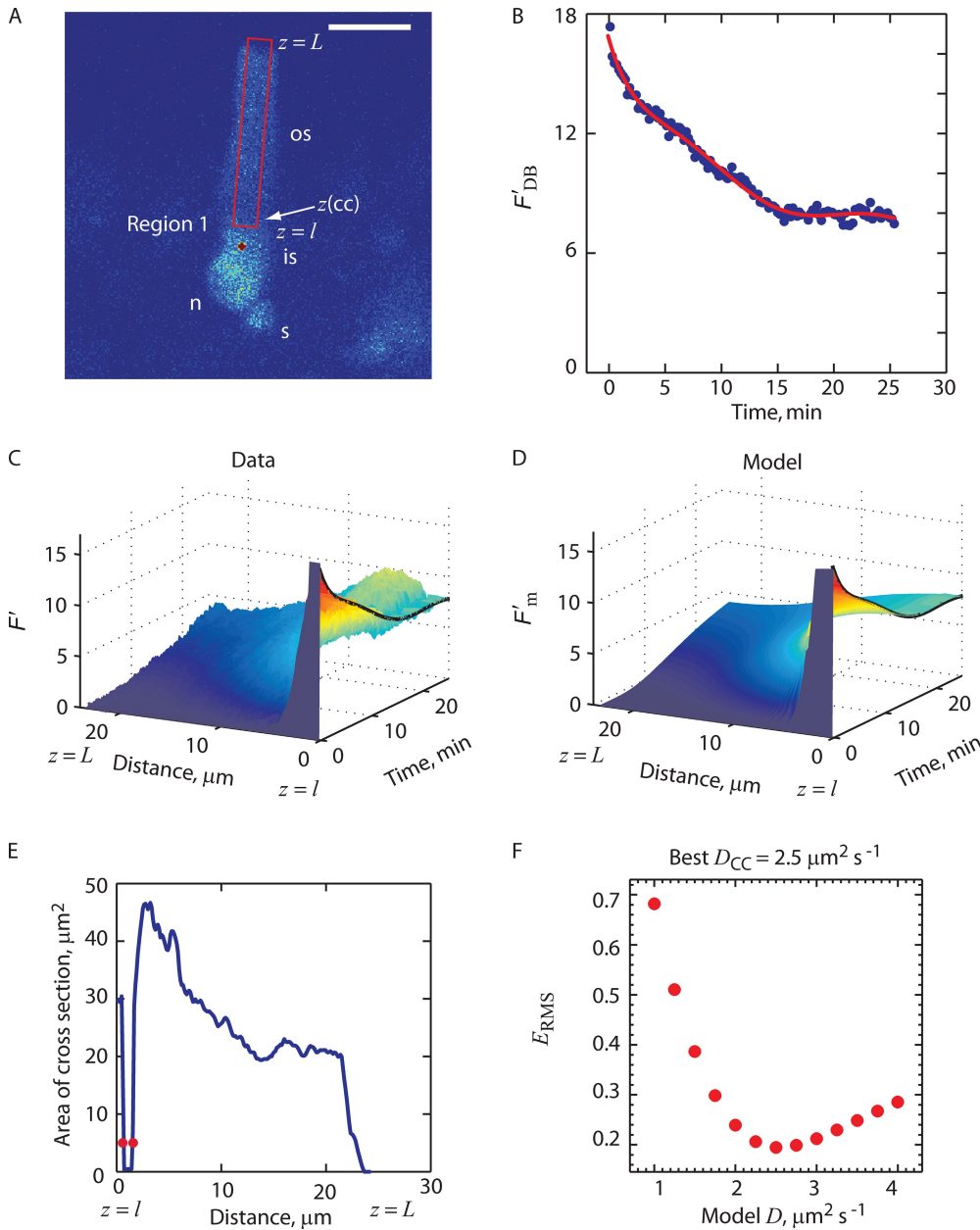


Figure 11. Estimation of the axial diffusion coefficient of PAGFP within the CC using the 1-D model. (A) Region over which the fluorescence was averaged in the radial dimension from each time course image to produce the spatiotemporal fluorescence profile shown in C. Note that in this case the region begins at an axial position just proximal to the CC, $z(cc)$. (B) To produce the Dirichlet BC the proximal five pixels in the region were averaged and fitted as described in Fig. 10. (C) Spatiotemporal map of fluorescence changes along the axial extent of the region shown in A. (D) Model prediction $F'_m(z,t)$ that best fitted the data. Eqs. 13–15 were solved with spatially varying $D(z)$: $D(z = IS)$, $5.2 \mu\text{m}^2 \text{s}^{-1}$; $D(z = OS)$, $0.08 \mu\text{m}^2 \text{s}^{-1}$; $D(z = CC)$ was varied to obtain the best fit of the model to the data. The thick black lines in C and D represent the Dirichlet boundary constraint. (E) Area of cross section versus axial distance profile, $A(z)$, for the region of the cell analyzed and which was used in Eq. 13 to calculate model profiles; note the sharp drop in A at the CC. The red symbols denote the transitions between IS and CC ($z(CC_i)$; left symbol) and the CC and OS ($z(CC_L)$; right symbol), and define the ranges over which $D(z)$ values described in D were applied. (F) RMS error values plotted as a function of D_{CC} .

(Fig. 2) (cf. Rosenkranz, 1977). The impact of tortuosity on D_{OS} may be predicted from a straightforward relation (Lamb et al., 1981):

$$\tau = \frac{F_V}{F_A}. \quad (26)$$

Here, F_V is of the fraction of the OS volume occupied by the discs, and F_A is the fraction of the cross section accessible to molecular diffusion (Lamb et al., 1981; Olson and Pugh, 1993). F_V has long been estimated to be ~ 0.5 (Rosenkranz, 1977; see also Peet et al., 2004), although a recent cryoelectron microscopy study of mouse rods suggests it could be as low as 0.3 (Nickell et al., 2007). F_A is determined by the gap between the discs and the plasma membrane (10–20 nm), and by

the incisures, infoldings of the plasma membrane that invaginate the discs (Fig. 12). On average, a frog disc contains 27 incisures with lengths of 2.7 μm (Tsukamoto, 1987) and gaps of ~ 10 nm (according to measurements made in salamander; Olson and Pugh, 1993). Accordingly, the area of a 7- μm diameter frog rod OS available for axial diffusion is $\sim 1.0 \mu\text{m}^2$, 2.6% of the OS cross-sectional area. Thus, Eq. 23 gives $\tau = 0.5/0.026 \sim 20$, and so predicts that tortuosity alone should reduce axial PAGFP diffusion 20-fold from D_{aq} . If the incisures were inaccessible to PAGFP diffusion, Eq. 26 would yield $\tau \sim 40$. Removing the contribution of tortuosity, we are left with an unaccounted 28- to 56-fold reduction in D_{OS} from D_{aq} , and 6- to 12-fold reduction from D_{CHO} (Table III).

Mechanisms underlying the retarded diffusion of PAGFP in the rod

GFP and its variants, particularly EGFP, have been used in benchmark studies of protein diffusion in cellular aqueous compartments (for review see Verkman, 2002; see also Dix and Verkman, 2008). We have recently shown that the GFP variant used here, PAGFP, is indistinguishable from EGFP with respect to its diffusion in aqueous solutions of varied viscosity and in CHO cells, but provided substantially superior performance with respect to signal/noise and light load (Calvert et al., 2007). The diffusion coefficient of GFP variants in aqueous compartments of cultured cells is generally reduced approximately three- to fivefold from its value in water or physiological saline (Swaminathan et al., 1997; Partikian et al., 1998; Dayel et al., 1999; Calvert et al., 2007). It is thus striking that PAGFP diffusion is much more retarded in the aqueous compartments of rods (Table III) than in those of most cells previously investigated (for exceptions, see Elowitz et al., 1999; Konopka et al., 2009), and calls for some explanation.

Retarded diffusion of macromolecules, including GFP variants, in aqueous compartments of cells has been ascribed primarily to four factors: fluid-phase cytoplasmic viscosity, macromolecular crowding, binding interactions, and hydrodynamic boundary effects (Hou et al., 1990; Kao et al., 1993; Minton, 1997; Luby-Phelps, 2000; Verkman, 2002; Dix and Verkman, 2008; Zhou et al., 2008). The viscosity of the aqueous cytoplasm is governed by the concentration of small solutes and organizing effects of macromolecules on water (Clegg, 1984; Parsegian and Rau, 1984). Crowding reduces the volume fraction available for translational diffusion and thus the number of possible paths available to a diffusing molecule. Binding interactions include all inelastic collisions of the diffuser with nonsolvent particles and intracellular surfaces (e.g., ER and SER) and microfilaments. Retarding hydrodynamic friction occurs when a significant fraction of the paths available to the diffuser are put in close contact with solvent that is less mobile. (These factors are not completely distinct; see the citations just given.)

The retardation of PAGFP diffusion by several of these factors could be greater in photoreceptors than in previously investigated cells (e.g., CHO cells). Photoreceptors may use a relatively high density of cytoskeletal elements to maintain their highly structured, polarized morphology. Crowding by macromolecules may be exceptionally high in the cytoplasm of the IS and OS: interferometric measurements of cytoplasm, which probe particulate density, indicate that the refractive index of the OS is 1.41 (Sidman, 1957) and the core of the myoid region of cones has an index of 1.42 (Rowe et al., 1996). These values contrast with those of cultured mammalian cells, with reported refractive indices in the 1.36 to 1.37 range (Lanni et al., 1985). The high refractive index in the OS is due to dense packing of lipids and phototransduction

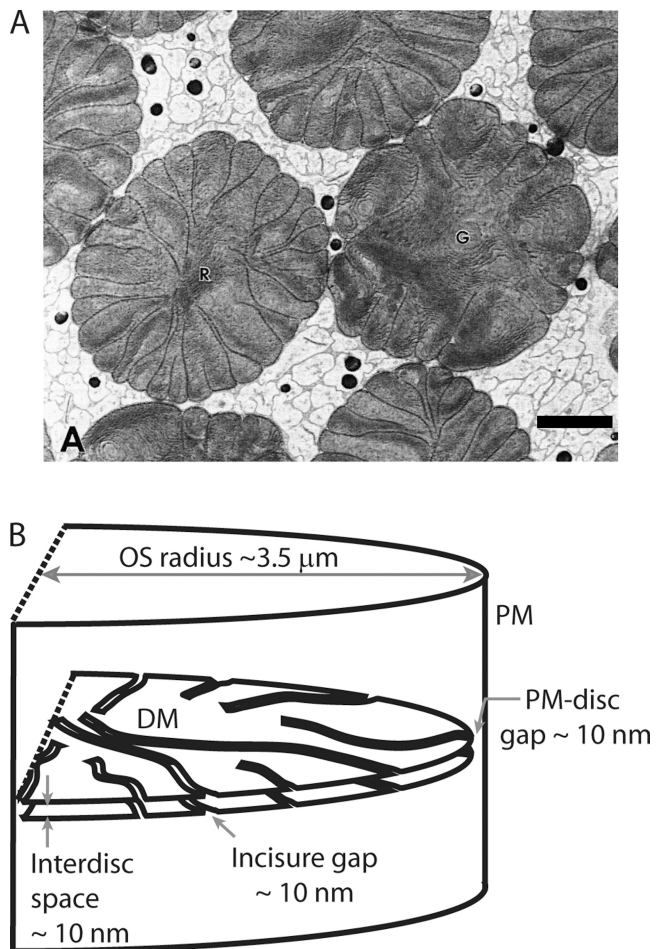


Figure 12. Morphology of OS discs. (A) Enface transmission electron micrographs of discs in the OSs of the bull frog *Rana catesbeiana*. Bar, 1.5 μm . Discs in rod photoreceptors have a scalloped morphology formed by infoldings called “incisures” that penetrate deep into their radial dimension. R, red rod; G, green rod. Image reprinted from Tsukamoto (1987) with permission from Elsevier. (B) Schematic of half of a rod OS, showing two disc membranes (DM) and the plasma membrane (PM) architecture. Average measurements used to calculate the patent area of cross section available for axial diffusion of molecules are indicated.

proteins, and in the IS it may reflect denser packing of protein-synthetic machinery needed to support the high turnover of phototransduction components in the OS, which, in the case of frogs, renews $\sim 2\%$ of its large complement of proteins daily (Young, 1967). Finally, the lamellar membranes of the OS and the putative high density cytoskeletal components offer an increased surface area that may retard the diffusion of PAGFP by weak binding interactions or hydrodynamic friction.

Strong binding interactions between PAGFP and subcellular structures do not appear to be involved because in the cells examined, the diffusion coefficients in the CC and OS did not correlate with the concentration of expressed PAGFP, which varied more than 200-fold in the rods investigated (see supplemental text). Another possible mechanism for slowed diffusion of PAGFP is

self-crowding. However, the highest expression level in the cells examined was $\sim 100 \mu\text{M}$, at least 10-fold below the theoretical threshold for crowding effects (see supplemental text).

The value of D_{OS} ($0.079 \mu\text{m}^2 \text{s}^{-1}$) reported here for PAGFP differs considerably from the value ($3.3 \mu\text{m}^2 \text{s}^{-1}$) recently reported for EGFP expressed in *Xenopus* rods (Wang et al., 2008). Several factors may explain this discrepancy, including the harsh conditions used to isolate the cells and an inadequate description of the FRAP bleach pattern. The manipulations used by Wang et al. (2008) to isolate, immobilize, and permeabilize the cells could cause cell swelling (increasing the water space) and depolymerization of cytoskeleton components (decreasing crowding). Our approach strictly maintains physiological intactness of the photoreceptors, as we imaged only rods that were in retinal slices and maintained normal morphology. The diffusion model applied by Wang et al. (2008) assumes uniform bleaching along the entire width of the rod OS, which was fixed to the coverslip. However, both bleaching and scanning were performed at a single focus level with a 1.3-NA oil-immersion objective. The radius of the diffraction-limited illumina-

tion volume along the axis of focus (the Rayleigh or Abbe limit) is $r = \lambda/NA^2 \sim 0.3 \mu\text{m}$ at 488 nm. Given an average *Xenopus* rod diameter of $6-7 \mu\text{m}$, a substantial fraction of the OS width would have been minimally bleached; therefore, the fluorescence recovery signals were likely much sped up by unbleached molecules diffusing radially into the scan plane from out of focus regions (cf. Figs. 6, 7, and 9).

Could advection due to active transport within the CC contribute to soluble PAGFP movement into the OS?

An alternative mechanism to diffusive transport of PAGFP to the OS compartment that warrants consideration is transport by advective flow of cytoplasm that may be generated by motor-based transport carriers. At a concentration of $\sim 3 \mu\text{M}$ in the OS, rhodopsin is the most abundant protein in the rod and, given the well-established rate of renewal of the OS disc membranes ($\sim 14 \text{ d}$ in *Xenopus*), can be estimated to be transported to the OS compartment via post-Golgi vesicles at a maximal rate of approximately one $\sim 300\text{-nm}$ diameter vesicle per second. It is controversial whether these vesicles transit the CC to reach the OS, or rather

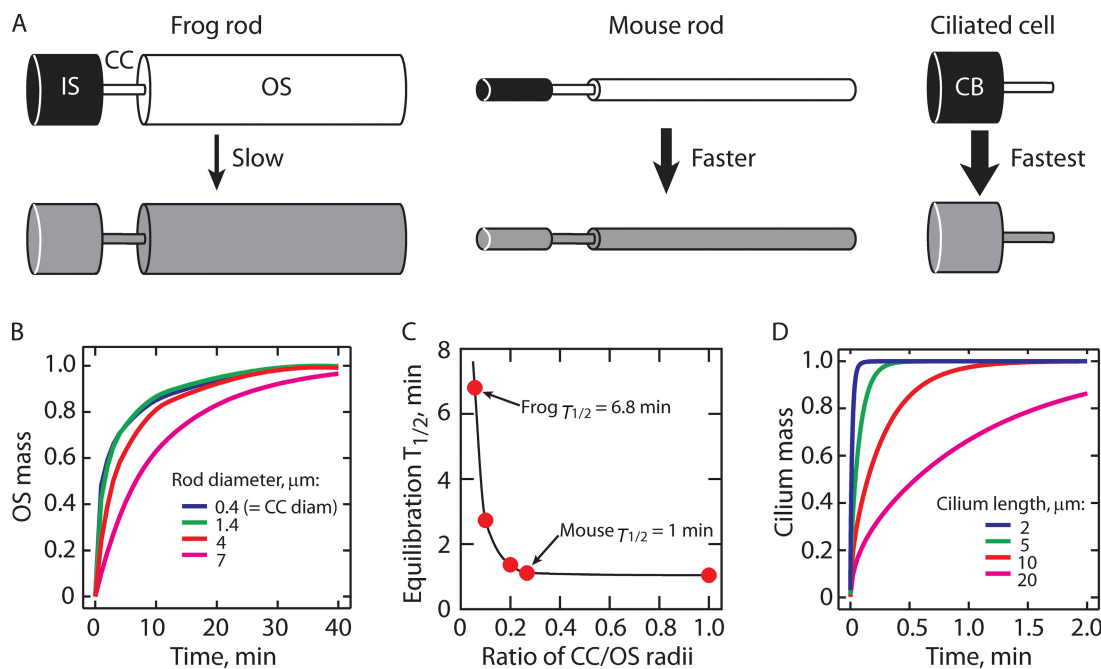


Figure 13. Impact of changes in areas of cross section on equilibration kinetics: predictions from the diffusion model. (A) Idealized cells with the geometry of frog or mouse rods and for an idealized ciliated cell for which equilibration time courses were modeled by solving Eqs. 13–15. The rod ISs or the cell body (CB) were initially uniformly filled with diffusing substance (black), and the OS and cilia were empty. Equilibration after some period of time is indicated by uniform gray in all compartments. Arrow thickness denotes relative speed of equilibration (see B–D). (B) Time courses of equilibration into rod OS compartments. The lengths of each compartment were: IS, $5 \mu\text{m}$; CC, $0.8 \mu\text{m}$; OS, $25 \mu\text{m}$. The CC had the same diameter in all cases, $0.4 \mu\text{m}$ (average diameter from Table I). A range of rod IS and OS diameters were modeled, including $7 \mu\text{m}$, representative of frog rods, and $1.4 \mu\text{m}$, based on the most recent measurements of mouse rod dimensions (Daniele et al., 2005). In all cases, $D_{\text{IS}} = 5 \mu\text{m}^2 \text{s}^{-1}$, $D_{\text{CC}} = 2 \mu\text{m}^2 \text{s}^{-1}$, and $D_{\text{OS}} = 0.1 \mu\text{m}^2 \text{s}^{-1}$. The mass in the OS normalized to the equilibrated OS mass is plotted. (C) Dependence of the $T_{1/2}$ of equilibration on the ratio of CC and IS–OS radii. Line is drawn through the points. (D) Time course of cilium equilibration. Ciliated cells ($10\text{-}\mu\text{m}$ long cell body and $5 \mu\text{m}$ in diameter, possessing a cilium $0.4 \mu\text{m}$ in diameter and varied length) were modeled. The mass of the diffusing substance in the cilium normalized to the equilibrated mass is plotted for cilia of indicated length.

fuse with the plasma membrane in the IS near the cilium transition zone and are carried to the OS via IFT. However, if the mechanism of transport of rhodopsin-laden membrane were shown to be motor-based movement of vesicles through the core of the CC, the ~300-nm diameter vesicles would be large enough to occlude most of the CC lumen, and could possibly produce a peristaltic flow of cytoplasm toward the OS. To examine the possibility of such an “advective” transport of PAGFP, the 1-D model of diffusion in the rod cell described in Theory was extended to include an advective term. This advection/diffusion model predicts that the steady-state PAGFP concentration in the OS compartment would exceed that in the IS compartment by >30% (see supplemental text). Contrary to this prediction, in none of the cells examined in the present paper, nor in the large population expressing EGFP examined in a previous paper (Peet, et al. 2004), did the steady-state concentration of PAGFP or EGFP in the OS compartment exceed that of the IS. It is thus unlikely that advection plays a significant role in the transport of soluble proteins between rod photoreceptor compartments.

Impact of variation in cell dimensions on the time course of soluble protein equilibration

Although diffusivities govern the local movements of protein in the cells, the overall time to equilibrate is greatly affected by cellular and subcellular dimensions. Consider the cases of frog and mouse rod photoreceptors. The CC of frog and mouse rods are the same diameter, yet the diameter of the cells are very different: frog rods are on average ~7 μm in diameter, whereas those of mice are ~1.4 μm . As a consequence, the frog rod cilium involves an ~330-fold reduction in the cross section available for diffusion, whereas the corresponding reduction in the mouse rod is only ~19-fold. In a three-compartment simulation, these differences resulted in equilibration times that differ approximately sevenfold (Fig. 13).

We similarly examined the equilibration time predicted for a ciliated epithelial cell where the cilium diameter is constant but attached to a large cytoplasmic reservoir, as, for example, for an olfactory cilium (cf. Fig. 1). Assuming the diffusion coefficients of the cell body and the cilium to be equal and ~5 $\mu\text{m}^2 \text{s}^{-1}$, the equilibration was remarkably fast (Fig. 13 D). Although the equilibration time varied significantly with cilium length, equilibration half-times were <1 min for lengths up to 20 μm (Fig. 13 D), suggesting that diffusion could be a viable means of soluble protein transport into all primary cilia.

The authors wish to thank Drs. Mohammad Haeri and Barry Knox for valuable assistance in generating transgenic *Xenopus*, Dr. Kathy Battaglia and Cheryl Gretzula for plasmid preparation, and Jason Stewart for valuable technical assistance.

P.D. Calvert is recipient of a Career Development Award from Research to Prevent Blindness (RPB). This work was supported by the Lions Clubs of Central New York and by grants from the Karl Kirchgessner Foundation (to P.D. Calvert) and the National Institutes of Health (grant EY018421 to P.D. Calvert and grants EY016453 and EY02660 to E.N. Pugh). The SUNY UMU Department of Ophthalmology is the recipient of an unrestricted grant from RPB.

Alan S. Verkman served as guest editor. (Journal policy regarding manuscripts submitted by the Editor or Associate Editors is available at <http://jgp.rupress.org/misc/policies.shtml#submitted>.)

Submitted: 31 August 2009

Accepted: 2 February 2010

REFERENCES

- Badano, J.L., N. Mitsuma, P.L. Beales, and N. Katsanis. 2006. The ciliopathies: an emerging class of human genetic disorders. *Annu. Rev. Genomics Hum. Genet.* 7:125–148. doi:10.1146/annurev.genom.7.080505.115610
- Besharse, J.C., D.M. Forestner, and D.M. Defoe. 1985. Membrane assembly in retinal photoreceptors. III. Distinct membrane domains of the connecting cilium of developing rods. *J. Neurosci.* 5:1035–1048.
- Blacque, O.E., E.A. Perens, K.A. Boroevich, P.N. Inglis, C. Li, A. Warner, J. Khattri, R.A. Holt, G. Ou, A.K. Mah, et al. 2005. Functional genomics of the cilium, a sensory organelle. *Curr. Biol.* 15:935–941. doi:10.1016/j.cub.2005.04.059
- Broekhuyse, R.M., E.F. Tolhuizen, A.P. Janssen, and H.J. Winkens. 1985. Light induced shift and binding of S-antigen in retinal rods. *Curr. Eye Res.* 4:613–618. doi:10.3109/02713688508999993
- Brown, E.B., E.S. Wu, W. Zipfel, and W.W. Webb. 1999. Measurement of molecular diffusion in solution by multiphoton fluorescence photobleaching recovery. *Biophys. J.* 77:2837–2849. doi:10.1016/S0006-3495(99)77115-8
- Calvert, P.D., K.J. Strissel, W.E. Schiesser, E.N. Pugh Jr., and V.Y. Arshavsky. 2006. Light-driven translocation of signaling proteins in vertebrate photoreceptors. *Trends Cell Biol.* 16:560–568. doi:10.1016/j.tcb.2006.09.001
- Calvert, P.D., J.A. Peet, A. Bragin, W.E. Schiesser, and E.N. Pugh Jr. 2007. Fluorescence relaxation in 3D from diffraction-limited sources of PAGFP or sinks of EGFP created by multiphoton photoconversion. *J. Microsc.* 225:49–71. doi:10.1111/j.1365-2818.2007.01715.x
- Clegg, J.S. 1984. Intracellular water and the cytomatrix: some methods of study and current views. *J. Cell Biol.* 99:167s–171s. doi:10.1083/jcb.99.1.167s
- Crank, J. 1975. The Mathematics of Diffusion. Second edition. Oxford University Press, New York. 424 pp.
- Daniele, L.L., C. Lillo, A.L. Lyubarsky, S.S. Nikonov, N. Philp, A.J. Mears, A. Swaroop, D.S. Williams, and E.N. Pugh Jr. 2005. Cone-like morphological, molecular, and electrophysiological features of the photoreceptors of the Nrl knockout mouse. *Invest. Ophthalmol. Vis. Sci.* 46:2156–2167. doi:10.1167/iov.04-1427
- Davis, E.E., M. Brueckner, and N. Katsanis. 2006. The emerging complexity of the vertebrate cilium: new functional roles for an ancient organelle. *Dev. Cell.* 11:9–19. doi:10.1016/j.devcel.2006.06.009
- Dayel, M.J., E.F. Hom, and A.S. Verkman. 1999. Diffusion of green fluorescent protein in the aqueous-phase lumen of endoplasmic reticulum. *Biophys. J.* 76:2843–2851. doi:10.1016/S0006-3495(99)77438-2
- Deane, J.A., D.G. Cole, E.S. Seeley, D.R. Diener, and J.L. Rosenbaum. 2001. Localization of intraflagellar transport protein IFT52 identifies basal body transitional fibers as the docking

- site for IFT particles. *Curr. Biol.* 11:1586–1590. doi:10.1016/S0960-9822(01)00484-5
- Dix, J.A., and A.S. Verkman. 2008. Crowding effects on diffusion in solutions and cells. *Annu Rev Biophys.* 37:247–263. doi:10.1146/annurev.biophys.37.032807.125824
- Elowitz, M.B., M.G. Surette, P.E. Wolf, J.B. Stock, and S. Leibler. 1999. Protein mobility in the cytoplasm of Escherichia coli. *J. Bacteriol.* 181:197–203.
- Flock, A., and A.J. Duvall III. 1965. The ultrastructure of the kinocilium of the sensory cells in the inner ear and lateral line organs. *J. Cell Biol.* 25:1–8. doi:10.1083/jcb.25.1.1
- Ganote, C.E., J.J. Grantham, H.L. Moses, M.B. Burg, and J. Orloff. 1968. Ultrastructural studies of vasopressin effect on isolated perfused renal collecting tubules of the rabbit. *J. Cell Biol.* 36:355–367. doi:10.1083/jcb.36.2.355
- Hou, L., F. Lanni, and K. Luby-Phelps. 1990. Tracer diffusion in F-actin and Ficoll mixtures. Toward a model for cytoplasm. *Biophys. J.* 58:31–43. doi:10.1016/S0006-3495(90)82351-1
- Jensen, C.G., C.A. Poole, S.R. McGlashan, M. Marko, Z.I. Issa, K.V. Vujcich, and S.S. Bowser. 2004. Ultrastructural, tomographic and confocal imaging of the chondrocyte primary cilium in situ. *Cell Biol. Int.* 28:101–110. doi:10.1016/j.cellbi.2003.11.007
- Kao, H.P., J.R. Abney, and A.S. Verkman. 1993. Determinants of the translational mobility of a small solute in cell cytoplasm. *J. Cell Biol.* 120:175–184. doi:10.1083/jcb.120.1.175
- Konopka, M.C., K.A. Sochacki, B.P. Bratton, I.A. Shkel, M.T. Record, and J.C. Weisshaar. 2009. Cytoplasmic protein mobility in osmotically stressed Escherichia coli. *J. Bacteriol.* 191:231–237. doi:10.1128/JB.00536-08
- Kozminski, K.G., P.L. Beech, and J.L. Rosenbaum. 1995. The Chlamydomonas kinesin-like protein FLA10 is involved in motility associated with the flagellar membrane. *J. Cell Biol.* 131:1517–1527. doi:10.1083/jcb.131.6.1517
- Kroll, K.L., and E. Amaya. 1996. Transgenic Xenopus embryos from sperm nuclear transplants reveal FGF signaling requirements during gastrulation. *Development.* 122:3173–3183.
- Kulaga, H.M., C.C. Leitch, E.R. Eichers, J.L. Badano, A. Lesemann, B.E. Hoskins, J.R. Lupski, P.L. Beales, R.R. Reed, and N. Katsanis. 2004. Loss of BBS proteins causes anosmia in humans and defects in olfactory cilia structure and function in the mouse. *Nat. Genet.* 36:994–998. doi:10.1038/ng1418
- Lamb, T.D., P.A. McNaughton, and K.W. Yau. 1981. Spatial spread of activation and background desensitization in toad rod outer segments. *J. Physiol.* 319:463–496.
- Lanni, F., A.S. Waggoner, and D.L. Taylor. 1985. Structural organization of interphase 3T3 fibroblasts studied by total internal reflection fluorescence microscopy. *J. Cell Biol.* 100:1091–1102. doi:10.1083/jcb.100.4.1091
- Liu, Q., G. Tan, N. Levenkova, T. Li, E.N. Pugh Jr., J.J. Rux, D.W. Speicher, and E.A. Pierce. 2007. The proteome of the mouse photoreceptor sensory cilium complex. *Mol. Cell. Proteomics.* 6:1299–1317. doi:10.1074/mcp.M700054-MCP200
- Luby-Phelps, K. 2000. Cytoarchitecture and physical properties of cytoplasm: volume, viscosity, diffusion, intracellular surface area. *Int. Rev. Cytol.* 192:189–221. doi:10.1016/S0074-7696(08)60527-6
- Mani, S.S., S. Batni, L. Whitaker, S. Chen, G. Engbretson, and B.E. Knox. 2001. Xenopus rhodopsin promoter. Identification of immediate upstream sequences necessary for high level, rod-specific transcription. *J. Biol. Chem.* 276:36557–36565. doi:10.1074/jbc.M101685200
- Marszalek, J.R., X. Liu, E.A. Roberts, D. Chui, J.D. Marth, D.S. Williams, and L.S. Goldstein. 2000. Genetic evidence for selective transport of opsin and arrestin by kinesin-II in mammalian photoreceptors. *Cell.* 102:175–187. doi:10.1016/S0092-8674(00)00023-4
- Menco, B.P. 1997. Ultrastructural aspects of olfactory signaling. *Chem. Senses.* 22:295–311. doi:10.1093/chemse/22.3.295
- Menco, B.P., A.M. Cunningham, P. Qasba, N. Levy, and R.R. Reed. 1997. Putative odour receptors localize in cilia of olfactory receptor cells in rat and mouse: a freeze-substitution ultrastructural study. *J. Neurocytol.* 26:691–706.
- Minton, A.P. 1997. Influence of excluded volume upon macromolecular structure and associations in ‘crowded’ media. *Curr. Opin. Biotechnol.* 8:65–69. doi:10.1016/S0958-1669(97)80159-0
- Nair, K.S., S.M. Hanson, A. Mendez, E.V. Gurevich, M.J. Kennedy, V.I. Shestopalov, S.A. Vishnivetskiy, J. Chen, J.B. Hurley, V.V. Gurevich, and V.Z. Slepak. 2005. Light-dependent redistribution of arrestin in vertebrate rods is an energy-independent process governed by protein-protein interactions. *Neuron.* 46:555–567. doi:10.1016/j.neuron.2005.03.023
- Nickell, S., P.S. Park, W. Baumeister, and K. Palczewski. 2007. Three-dimensional architecture of murine rod outer segments determined by cryoelectron tomography. *J. Cell Biol.* 177:917–925. doi:10.1083/jcb.200612010
- Olson, A., and E.N. Pugh Jr. 1993. Diffusion coefficient of cyclic GMP in salamander rod outer segments estimated with two fluorescent probes. *Biophys. J.* 65:1335–1352. doi:10.1016/S0006-3495(93)81177-9
- Parsegian, V.A., and D.C. Rau. 1984. Water near intracellular surfaces. *J. Cell Biol.* 99:196s–200s. doi:10.1083/jcb.99.1.196s
- Partikian, A., B. Olveczky, R. Swaminathan, Y. Li, and A.S. Verkman. 1998. Rapid diffusion of green fluorescent protein in the mitochondrial matrix. *J. Cell Biol.* 140:821–829. doi:10.1083/jcb.140.4.821
- Patterson, G.H., and J. Lippincott-Schwartz. 2002. A photoactivatable GFP for selective photolabeling of proteins and cells. *Science.* 297:1873–1877. doi:10.1126/science.1074952
- Pazour, G.J., and J.L. Rosenbaum. 2002. Intraflagellar transport and cilia-dependent diseases. *Trends Cell Biol.* 12:551–555. doi:10.1016/S0962-8924(02)02410-8
- Pazour, G.J., B.L. Dickert, Y. Vucica, E.S. Seeley, J.L. Rosenbaum, G.B. Witman, and D.G. Cole. 2000. *Chlamydomonas IFT88* and its mouse homologue, polycystic kidney disease gene *tg737*, are required for assembly of cilia and flagella. *J. Cell Biol.* 151:709–718. doi:10.1083/jcb.151.3.709
- Pazour, G.J., N. Agrin, J. Leszyk, and G.B. Witman. 2005. Proteomic analysis of a eukaryotic cilium. *J. Cell Biol.* 170:103–113. doi:10.1083/jcb.200504008
- Peet, J.A., A. Bragin, P.D. Calvert, S.S. Nikonov, S. Mani, X. Zhao, J.C. Besharse, E.A. Pierce, B.E. Knox, and E.N. Pugh Jr. 2004. Quantification of the cytoplasmic spaces of living cells with EGFP reveals arrestin-EGFP to be in disequilibrium in dark adapted rod photoreceptors. *J. Cell Sci.* 117:3049–3059. doi:10.1242/jcs.01167
- Peters, K.R., G.E. Palade, B.G. Schneider, and D.S. Papermaster. 1983. Fine structure of a periciliary ridge complex of frog retinal rod cells revealed by ultrahigh resolution scanning electron microscopy. *J. Cell Biol.* 96:265–276. doi:10.1083/jcb.96.1.265
- Peterson, J.J., B.M. Tam, O.L. Moritz, C.L. Shelamer, D.R. Dugger, J.H. McDowell, P.A. Hargrave, D.S. Papermaster, and W.C. Smith. 2003. Arrestin migrates in photoreceptors in response to light: a study of arrestin localization using an arrestin-GFP fusion protein in transgenic frogs. *Exp. Eye Res.* 76:553–563. doi:10.1016/S0014-4835(03)00032-0
- Philp, N.J., W. Chang, and K. Long. 1987. Light-stimulated protein movement in rod photoreceptor cells of the rat retina. *FEBS Lett.* 225:127–132. doi:10.1016/0014-5793(87)81144-4
- Potma, E.O., W.P. de Boeij, L. Bosgraaf, J. Roelofs, P.J. van Haastert, and D.A. Wiersma. 2001. Reduced protein diffusion rate by cytoskeleton in vegetative and polarized dictyostelium cells. *Biophys. J.* 81:2010–2019. doi:10.1016/S0006-3495(01)75851-1

- Praetorius, H.A., and K.R. Spring. 2005. A physiological view of the primary cilium. *Annu. Rev. Physiol.* 67:515–529. doi:10.1146/annurev.physiol.67.040403.101353
- Rosenbaum, J.L., and G.B. Witman. 2002. Intraflagellar transport. *Nat. Rev. Mol. Cell Biol.* 3:813–825. doi:10.1038/nrm952
- Rosenkranz, J. 1977. New aspects of the ultrastructure of frog rod outer segments. *Int. Rev. Cytol.* 50:25–158. doi:10.1016/S0074-7696(08)60098-4
- Rowe, M.P., J.M. Corless, N. Engheta, and E.N. Pugh Jr. 1996. Scanning interferometry of sunfish cones. I. Longitudinal variation in single cone refractive index. *J. Opt. Soc. Am. A Opt. Image Sci. Vis.* 13:2141–2150. doi:10.1364/JOSAA.13.002141
- Schiesser, W.E. 1991. The numerical method of lines: integration of partial differential equations. Elsevier Academic Press, New York. 326 pp.
- Schiesser, W.E., and G.W. Griffiths. 2009. A compendium of partial differential equation models: method of lines analysis with MATLAB. Cambridge University Press, New York. 474 pp.
- Sidman, R.L. 1957. The structure and concentration of solids in photoreceptor cells studied by refractometry and interference microscopy. *J. Biophys. Biochem. Cytol.* 3:15–30.
- Strissel, K.J., P.V. Lishko, L.H. Trieu, M.J. Kennedy, J.B. Hurley, and V.Y. Arshavsky. 2005. Recoverin undergoes light-dependent intracellular translocation in rod photoreceptors. *J. Biol. Chem.* 280:29250–29255. doi:10.1074/jbc.M501789200
- Swaminathan, R., C.P. Hoang, and A.S. Verkman. 1997. Photobleaching recovery and anisotropy decay of green fluorescent protein GFP-S65T in solution and cells: cytoplasmic viscosity probed by green fluorescent protein translational and rotational diffusion. *Biophys. J.* 72:1900–1907. doi:10.1016/S0006-3495(97)78835-0
- Townes-Anderson, E., P.R. MacLeish, and E. Raviola. 1985. Rod cells dissociated from mature salamander retina: ultrastructure and uptake of horseradish peroxidase. *J. Cell Biol.* 100:175–188. doi:10.1083/jcb.100.1.175
- Trojan, P., N. Krauss, H.W. Choe, A. Giessl, A. Pulvermüller, and U. Wolfrum. 2008. Centrins in retinal photoreceptor cells: regulators in the connecting cilium. *Prog. Retin. Eye Res.* 27:237–259. doi:10.1016/j.preteyeres.2008.01.003
- Tsukamoto, Y. 1987. The number, depth and elongation of disc incisions in the retinal rod of *Rana catesbeiana*. *Exp. Eye Res.* 45:105–116. doi:10.1016/S0014-4835(87)80082-9
- Verkman, A.S. 2002. Solute and macromolecule diffusion in cellular aqueous compartments. *Trends Biochem. Sci.* 27:27–33. doi:10.1016/S0968-0004(01)02003-5
- Vollrath, M.A., K.Y. Kwan, and D.P. Corey. 2007. The micro-machinery of mechanotransduction in hair cells. *Annu. Rev. Neurosci.* 30:339–365. doi:10.1146/annurev.neuro.29.051605.112917
- Wang, Q.X., L. Zhang, F. Zhang, G. He, M. Zhang, T. Jamrich, and G. Wensel. 2008. Activation-dependent hindrance of photoreceptor G protein diffusion by lipid microdomains. *J. Biol. Chem.* 283:30015–30024.
- Wolfrum, U., A. Giessl, and A. Pulvermüller. 2002. Centrins, a novel group of Ca²⁺-binding proteins in vertebrate photoreceptor cells. *Adv. Exp. Med. Biol.* 514:155–178.
- Young, R.W. 1967. The renewal of photoreceptor cell outer segments. *J. Cell Biol.* 33:61–72. doi:10.1083/jcb.33.1.61
- Zhou, H.X., G. Rivas, and A.P. Minton. 2008. Macromolecular crowding and confinement: biochemical, biophysical, and potential physiological consequences. *Annu. Rev. Biophys.* 37:375–397. doi:10.1146/annurev.biophys.37.032807.125817
- Zipfel, W.R., R.M. Williams, and W.W. Webb. 2003. Nonlinear magic: multiphoton microscopy in the biosciences. *Nat. Biotechnol.* 21:1369–1377. doi:10.1038/nbt899

SUPPLEMENTAL MATERIAL

Calvert et al., <http://www.jgp.org/cgi/content/full/jgp.200910322/DC1>

METHODS AND VERIFICATION OF THE NUMERICAL SOLUTIONS OF THE DIFFUSION EQUATIONS

The details of the numerical solutions of the 3-D diffusion equations in a right-circular cylinder and in one spatial dimension with continuously variable area of cross section and D are presented here. Several tests of the accuracy of the numerical methods are also presented.

Numerical solution of the 3-D model

Theory Eqs. 2 and 3 are parabolic partial differential equations (PDEs) with unspecified coordinates. Rods, in particular their OSs, are approximately right-circular cylinders; thus, solution of Eqs. 2–7 with respect to rods is most conveniently done in cylindrical coordinates. The PDEs describing the diffusion of the unphotoconverted, b , and photoconverted, c , forms of PAGFP with respect to an inhomogeneous source term in cylindrical coordinates are

$$\frac{\partial b}{\partial t} = D_r \left(\frac{\partial^2 b}{\partial r^2} + \frac{1}{r} \frac{\partial b}{\partial r} \right) + D_\theta \frac{1}{r^2} \left(\frac{\partial^2 b}{\partial \theta^2} \right) + D_z \left(\frac{\partial^2 b}{\partial z^2} \right) - Q_s \quad (\text{S1})$$

$$\frac{\partial c}{\partial t} = D_r \left(\frac{\partial^2 c}{\partial r^2} + \frac{1}{r} \frac{\partial c}{\partial r} \right) + D_\theta \frac{1}{r^2} \left(\frac{\partial^2 c}{\partial \theta^2} \right) + D_z \left(\frac{\partial^2 c}{\partial z^2} \right) + Q_s, \quad (\text{S2})$$

where D_r , D_θ , and D_z are the diffusivities in the indicated directions.

Eqs. S1 and S2 are first order in t and second order in r , θ , and z . Therefore, one initial condition (IC) in t and two BCs (BCs) in each of the spatial variables r , θ , and z are required for each equation. The ICs given in Eq. 5 are restated here in cylindrical coordinates:

$$b(r, \theta, z, t \leq 0) = b_0 \quad (\text{S3})$$

$$c(r, \theta, z, t \leq 0) = 0. \quad (\text{S4})$$

The BCs in r were taken as:

$$\frac{\partial b(r=0, \theta, z, t)}{\partial r} = \frac{\partial b(r=r_0, \theta, z, t)}{\partial r} = 0 \quad (\text{S5a,b})$$

$$\frac{\partial c(r=0, \theta, z, t)}{\partial r} = \frac{\partial c(r=r_0, \theta, z, t)}{\partial r} = 0, \quad (\text{S6a,b})$$

which specify symmetry in r at $r=0$ and specify a no-flux boundary at the cell surface, $r=r_0$. The BCs in θ are:

$$\frac{\partial b(r, \theta=0, z, t)}{\partial \theta} = \frac{\partial b(r, \theta=\pi/2, z, t)}{\partial \theta} = 0 \quad (\text{S7a,b})$$

$$\frac{\partial c(r, \theta=0, z, t)}{\partial \theta} = \frac{\partial c(r, \theta=\pi/2, z, t)}{\partial \theta} = 0, \quad (\text{S8a,b})$$

which specify symmetry in θ at $\theta=0, \pi/2$ due to the symmetry of the source term and assuming isotropic diffusion in r and θ . The BCs in z are:

$$\frac{\partial b(r, \theta, z=l, t)}{\partial z} = \frac{\partial b(r, \theta, z=L, t)}{\partial z} = 0 \quad (\text{S9a,b})$$

$$\frac{\partial c(r, \theta, z=l, t)}{\partial z} = \frac{\partial c(r, \theta, z=L, t)}{\partial z} = 0, \quad (\text{S10a,b})$$

which specify a no-flux condition at the ends of the cylinder, $z=l, L$ (compare Fig. 2 B).

The numerical solution to Eqs. S1–S10 is accomplished through the method of lines (MOL), which replaces the PDEs specified by Eqs. S1 and S2 with ODE (finite difference) approximations of the derivatives with respect to r , θ , and z (Schiesser, 1991; Schiesser and Griffiths, 2009). To develop a numerical procedure, the inherent singularities at $r=0$ in Eqs. S1 and S2 must be regularized. For example, the first singularity in the radial term of Eq. S1 can be handled in the conventional way using l'Hospital's rule and Eq. S5a

$$\lim_{r \rightarrow 0} \frac{1}{r} \frac{\partial b}{\partial r} = \frac{\partial^2 b}{\partial r^2}. \quad (\text{S11})$$

The second singularity in Eq. S1,

$$\lim_{r \rightarrow 0} \frac{1}{r^2} \left(\frac{\partial^2 b}{\partial \theta^2} \right),$$

appears not to have a readily available value in cylindrical coordinates. Thus, we reason that essentially what is required is the accurate calculation of the Laplacian (RHS) of Eq. S1 at the origin $r = 0$, which may be achieved in any suitable coordinate system. Therefore, we switch to Cartesian coordinates, in which there is a solution at $r = 0$, to accomplish this. The Laplacian in Cartesian coordinates is

$$\nabla^2 = \frac{\partial^2}{\partial x^2} + \frac{\partial^2}{\partial y^2} + \frac{\partial^2}{\partial z^2}. \quad (\text{S12})$$

For Eq. S1 at the general grid point $p(i,j,k)$, where i, j , and k are the indices for r, θ , and z , respectively, the spatial derivatives are approximated as

$$\begin{aligned} \frac{\partial^2 b}{\partial r^2} + \frac{1}{r} \frac{\partial b}{\partial r} &\approx \frac{b(i+1,j,k) - 2b(i,j,k) + b(i-1,j,k)}{\Delta r^2} + \\ &+ \frac{1}{r(i,j,k)} \cdot \frac{b(i+1,j,k) - b(i-1,j,k)}{2\Delta r} \end{aligned} \quad (\text{S13a})$$

$$\frac{1}{r^2} \frac{\partial^2 b}{\partial \theta^2} \approx \frac{1}{r(i,j,k)^2} \frac{b(i,j+1,k) - 2b(i,j,k) + b(i,j-1,k)}{\Delta \theta^2} \quad (\text{S13b})$$

$$\frac{\partial^2 b}{\partial z^2} \approx \frac{b(i,j,k+1) - 2b(i,j,k) + b(i,j,k-1)}{\Delta z^2} \quad (\text{S13c})$$

and the inhomogeneous source term is

$$\begin{aligned} Q_s &= \alpha_m^* \gamma^* I^m(i,j,k,t) b, & 0 \leq t \leq \Delta T \\ &= 0, & t \geq \Delta T. \end{aligned} \quad (\text{S13d})$$

Substitution of Eq. S13 in Eq. S1 gives a system of $n_r \times n_\theta \times n_z$ ODEs in t . The left-hand side of Eq. S1 is the derivative $db(i,j,k) / dt$, for which the IC is Eq. S3.

Numerical solution of the 1-D model with variable $A(z)$ and $D(z)$

The mass balance for a rod cell idealized as a 1-D cylinder, with axial coordinate z , variable diffusion coefficient $D(z)$, and cross-sectional area $A(z)$ (Eq. 13) may be expressed as:

$$A(z)\Delta z \frac{\partial c}{\partial t} = -A(z)D(z) \frac{\partial c}{\partial z} \Big|_z - \left[-A(z)D(z) \frac{\partial c}{\partial z} \Big|_{z+\Delta z} \right], \quad (\text{S14})$$

where $A(z)\Delta z \partial c / \partial t$ is the accumulation or depletion (depending on the sign of $\partial c / \partial t$) of protein in an incremental volume $A(z)\Delta z$, and $-A(z)D(z)\partial c / \partial z|_z$ is the rate of diffusion into or out of (depending on the sign of $\partial c / \partial z$) the infinitesimal spatial position z according to Fick's first law. Similarly, $-A(z)D(z)\partial c / \partial z|_{z+\Delta z}$ is the rate of diffusion into or out of the infinitesimal spatial position $z + \Delta z$. Thus, the difference in these two terms is the net rate of mass transfer into or out of the incremental volume due to diffusion. Division of Eq. S14 by $A(z)\Delta z$ with minor rearrangement gives

$$\frac{\partial c}{\partial t} = \frac{A(z)D(z) \frac{\partial c}{\partial z} \Big|_{z+\Delta z} - A(z)D(z) \frac{\partial c}{\partial z} \Big|_z}{A(z)\Delta z}. \quad (\text{S15})$$

In the limit $\Delta z \rightarrow 0$, Eq. S15 becomes

$$\frac{\partial c}{\partial t} = \frac{1}{A(z)} \frac{\partial \left[A(z)D(z) \frac{\partial c}{\partial z} \right]}{\partial z}. \quad (\text{S16})$$

Initial and BCs

Either of two sets of BCs were used in the solution of Eq. S16:

$$\frac{\partial c(0,t)}{\partial z} = \frac{\partial c(L,t)}{\partial z} = 0 \quad (\text{S17})$$

or

$$c(0,t) = f(t), \quad \frac{\partial c(L,t)}{\partial z} = 0. \quad (\text{S18})$$

The two homogeneous (0) Neumann BCs of Eq. S17 specify 0 flux of the protein through the boundaries at $z = 0, L$. The Dirichlet (first) BC of Eq. S18 specifies the concentration of the protein at $z = 0$ as a time-dependent function $f(t)$. The homogeneous Neumann (second) BC at $z = L$ specifies 0 flux of the protein through the boundary $z = L$. Finally, Eq. S16 also requires one IC, which is

$$c(z,0) = c_0(z), \quad (\text{S19})$$

where $c_0(z)$ is an initial distribution of the protein.

Solution

Eqs. S17–S19 were solved numerically by the MOL. The z dimension of the rod was divided into n spatial positions with index i , and the derivatives in z were approximated by finite differences, which converts them into algebraic expressions, leaving only the derivative in t . Thus, ODEs in t remain. At grid point i , the MOL approximation of Eq. S16 is

$$\frac{dc_i}{dt} = \frac{1}{A(z_i)} \cdot \left[\frac{A(z_{i+1})D(z_{i+1}) + A(z_i)D(z_i)}{2} \left(\frac{c_{i+1} - c_i}{z_{i+1} - z_i} \right) - \frac{A(z_i)D(z_i) + A(z_{i-1})D(z_{i-1})}{2} \left(\frac{c_i - c_{i-1}}{z_i - z_{i-1}} \right) \right] \cdot \left[\frac{1}{(z_{i+1} + z_i)/2 - (z_i + z_{i-1})/2} \right] \quad (\text{S20})$$

for $i=1,\dots,n$. For the first of the BCs (Eqs. S17 and S20) becomes

$$\frac{dc_1}{dt} = \frac{1}{A(z_1)} \cdot \left[\frac{A(z_2)D(z_2) + A(z_1)D(z_1)}{2} \left(\frac{c_2 - c_1}{z_2 - z_1} \right) \right] \cdot \left[\frac{1}{z_2 - z_1} \right], \quad (\text{S21})$$

where the flux between $i=0$ (a fictitious point) and $i=1$ is taken to be 0. Similarly, Eq. S20 for the no-flux BC of Eq. S17 at $z=L$ is

$$\frac{dc_n}{dt} = \frac{1}{A(z_n)} \cdot \left[-\frac{A(z_n)D(z_n) + A(z_{n-1})D(z_{n-1})}{2} \left(\frac{c_n - c_{n-1}}{z_n - z_{n-1}} \right) \right] \cdot \left[\frac{1}{z_n - z_{n-1}} \right], \quad (\text{S22})$$

where the flux between the fictitious point $i=n+1$ and $i=n$ is taken to be 0.

For the Dirichlet BC of Eq. S18 at $z=0$, the ODE at grid point $i=1$ is

$$\frac{dc_1}{dt} = \frac{df(t)}{dt}, \quad (\text{S23})$$

and the Neumann BC of Eq. S18 at $z=L$ is the same as Eq. S22.

The ODEs are integrated forward in t from $t=0$ using a MATLAB ODE integrator, e.g., ode15s, starting from the IC of Eq. S19.

Verification of the solutions

The numerical solutions obtained were verified using three criteria as follows.

Grid density: mass conservation

An important consideration in numerical approximations of PDE systems is the appropriate grid density. The density should be sufficient to provide an accurate solution, but not so dense that the time required to run the code becomes prohibitively long. Good indicators of accurate solutions are the maintenance of constant mass

of the diffusing substance and solution convergence over the time course of the calculation. The total mass of components b and c was computed by an approximation to the integral based on the differential volume $rd\theta dr dz$

$$M(t) = \int_0^L \int_0^{n_\theta} \int_0^{2\pi} [b(r, \theta, z, t) + c(r, \theta, z, t)] r d\theta dr dz \approx \sum_{k=1}^{n_z-1} \sum_{j=1}^{n_\theta-1} \sum_{i=1}^{n_r-1} [b(i, j, k) + b(i+1, j, k) + b(i, j+1, k) + b(i, j, k+1) + c(i, j, k) + c(i+1, j, k) + c(i, j+1, k) + c(i, j, k+1)] / 4[r(i) + r(i+1)] / 2\Delta\theta\Delta r\Delta z, \quad (\text{S24})$$

where $\Delta\theta$, Δr , and Δz are the finite difference increments in θ , r , and z , respectively.

We find that the most important consideration in determining appropriate grid density that maintains constant mass is that the source term (Q_s , Eq. 4) be adequately represented spatially with best results obtained when Q_s is at least eightfold over sampled in the radial and axial dimensions. In terms of the dimensions of the psf , which is described as a Gaussian profile with $\sigma_{x,z} = 0.16 \mu\text{m}$, this means the best results were obtained with a grid density of $8/0.32 = 25$ grid points per μm . At this density, mass was conserved to three significant figures.

As a matter of practicality, in a cylindrical OS 40- μm long with $r = 3 \mu\text{m}$, and θ sampled at 10-degree increments, the number of ODEs ($n_r \times n_\theta \times n_z$) calculated for each time point at this grid density was $75 \times 36 \times 1,000 = 2.7 \times 10^6$. Symmetry allows eightfold reduction in this number by calculating a single octant of the 3-D space.

Grid density: solution convergence

Solution accuracy was directly checked by varying the grid density in r , θ , and z . Increasing the density beyond that required for the mass balance did not materially improve the convergence beyond three significant figures.

Comparison to cases with tractable analytical solutions

To assess the accuracy of the numerical solutions, spatial geometries, ICs, and BCs may be chosen that allowed analytical solutions that then may be compared with the various solutions obtained by the MOL. In the case of the 3-D right-circular cylinder (Eqs. 2–7), relevant analytical solutions are most conveniently obtained via Green's functions with ICs defined by the Dirac delta function. Such solutions are readily found in Carslaw and Jaeger (1959) or Polyanin (2001). Comparisons of MOL to analytical solutions obtained as such have been

examined in detail previously and shown to be identical to three significant figures (Schiesser and Griffiths, 2009).

To test the accuracy of the numerical 1-D model described by Eqs. 13–15, we examined diffusion equations for a right-circular cylinder (constant $A(z)$, identical to the slab) with axial dimension, z , boundaries at $z = 0$ and $z = L$, and with the following initial and BCs:

$$\begin{aligned} c(z, t=0) &= 0 \\ c(z=0, t) &= f(t) \\ \frac{\partial c(z=L, t)}{\partial z} &= 0, \end{aligned} \quad (\text{S25})$$

where $f(t) = C(1 - \exp(-kt))$, C is the maximum concentration, and k is the time constant of concentration change. The diffusion equations with these ICs and BCs may be

solved using Duhamel's theorem, which allows analytical solution of PDEs with time-dependent terms. The solution is (Carslaw and Jaeger, 1959)

$$c(z, t) = C - C \exp(-kt) \frac{\cos(z(k/D)^{1/2})}{\cos(l(k/D)^{1/2})} - \frac{16kCl^2}{\pi} \sum_{n=0}^{\infty} \frac{(-1)^n \exp(-D(2n+1)^2 \pi^2 t / 4L^2)}{(2n+1)[4kL^2 - D\pi^2(2n+1)^2]} \cos \frac{(2n+1)\pi z}{2L}. \quad (\text{S26})$$

The numerical solution of Eqs. 13–15 with the BCs stated in Eq. S25 is identical to the analytical solution (Eq. S26) to three figures (Fig. S1). Additional verification procedures may be found in Calvert et al. (2007).

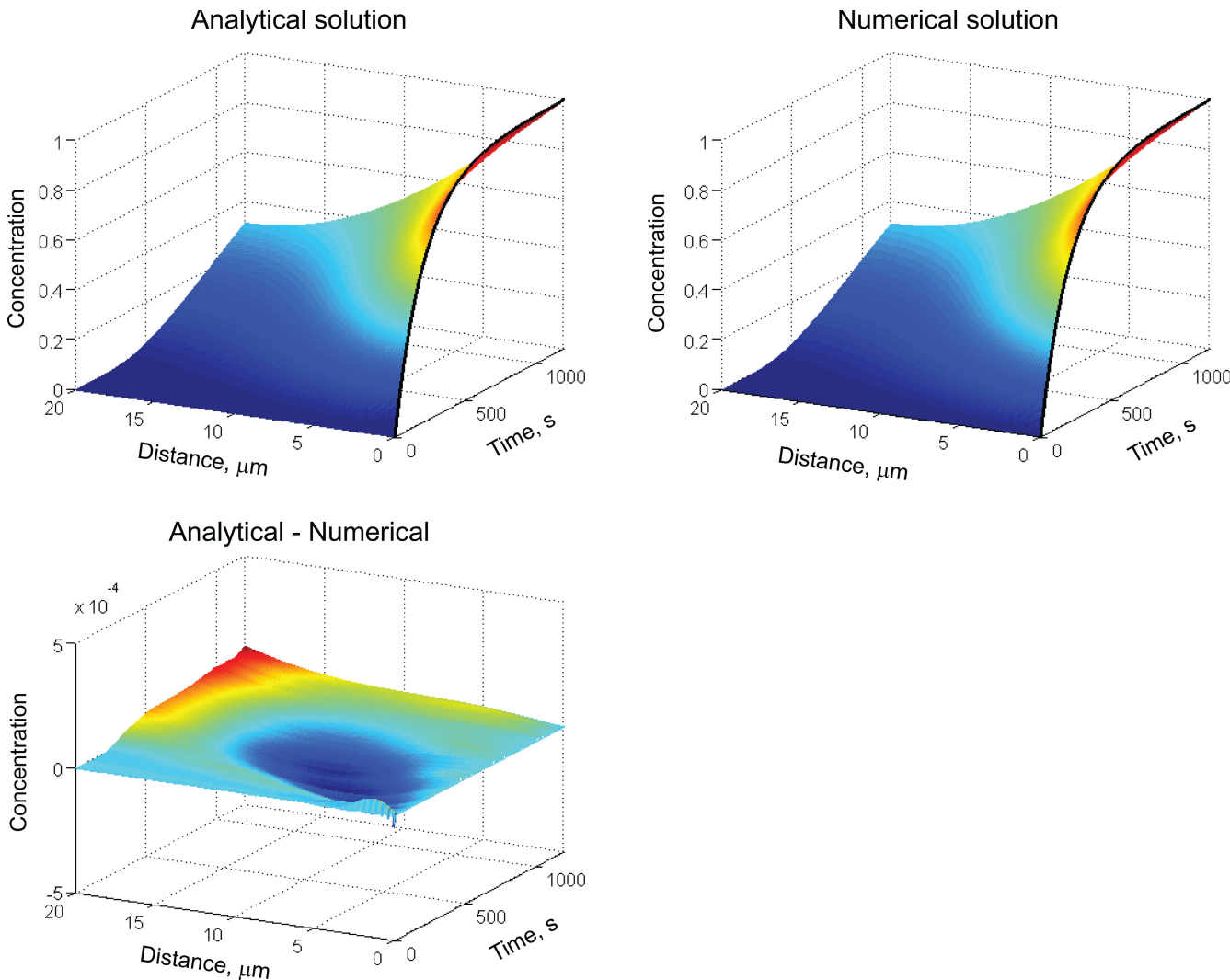


Figure S1. Comparison of analytical and numerical solutions to diffusion in a cylinder with a time varying Dirichlet BC at $z = 0$. The analytical solution used $k = 0.005 \text{ s}^{-1}$ and $C = 1$ in Eq. S26. The numerical solution used an exponential function with the same constants implemented as a Dirichlet BC; $D = 0.10 \mu\text{m}^2 \text{s}^{-1}$. The maximum absolute difference was 1.35×10^{-4} (0.0135%).

Data analysis details

RMS Error optimization of estimates of D . Estimates of diffusion coefficients were optimized by calculating the root-mean-square difference error E_{RMS} between fluorescence data and model prediction. In the case of the point blast line scan protocol of Fig. 9, where the 3-D cylinder model was used, this was calculated as

$$E_{RMS} = \left[\frac{\sum_r \sum_t (F'(r,t) - F_m(r,t))^2}{n_{pts}} \right]^{0.5}, \quad (\text{S27})$$

and in the case of the 1-D model, this was calculated as

$$E_{RMS} = \left[\frac{\sum_z \sum_t (F'(z,t) - F_M(z,t))^2}{n_{pts}} \right]^{0.5}, \quad (\text{S28})$$

where F' is the spatiotemporal profile of water space-corrected fluorescence, F_M is the fluorescence profile

predicted by the model, and n_{pts} is the total number of values in the spatiotemporal profile.

Determination of cell dimensions. Determination of the dimension of the cell being examined, particularly with respect to the CC and its relationship to the IS–OS transition, is crucial to the analysis of molecular diffusion. The dimensions of the cells were determined from 3-D scans of the cells at the beginning or end of a given experiment. The cell of interest was cut from the image stack using a 3-D “cookie-cutting” routine described previously (Peet et al., 2004). Individual intensity images in the x – z dimension (where here z refers to the direction of the optical path) were deconvolved with a kernel derived from the measured 3-D point spread function (psf) to remove the blurring inherent to confocal and multiphoton imaging, after which the edges of the cell were detected using the Canny method (available in the MATLAB Image Processing Toolbox). To obtain a cell’s area of cross section as a function of the axial, z dimension, the areas of the pixels identified as being within the cell boundary for each x – z image were integrated (Fig. S2).

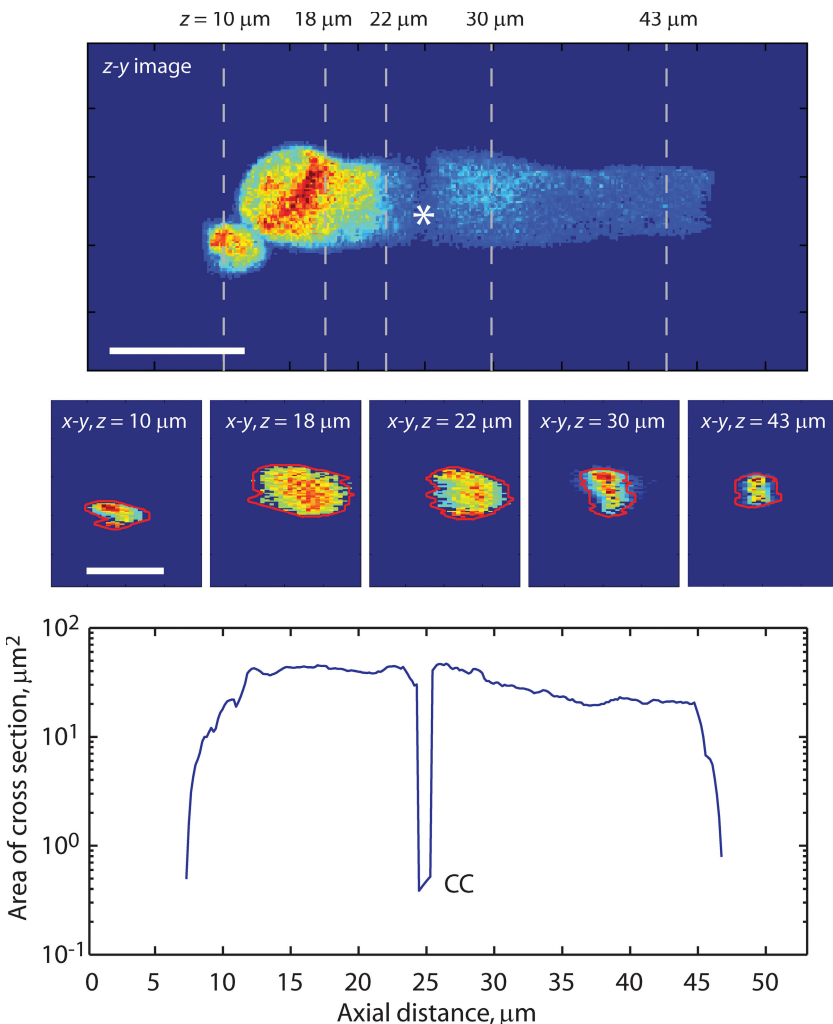


Figure S2. Determination of the area of cross section as a function of axial position. (Top) Central z – y image from a 3-D image stack of a rod expressing PAGFP. (Middle) x – y cross sections from the indicated z positions illustrate the edge detection protocol (red line). The areas of each pixel within the detected cross section are integrated to arrive at the area of cross section for a given z position. (Bottom) Logarithm of the areas of cross section plotted as a function of distance in z . CC indicates the area of cross section of the CC that was inserted at the IS–OS transition as determined by visual inspection of the projection image (indicated by white asterisk in top panel).

The cross section of the CC cannot be determined with confocal or multiphoton microscopy because its size is below the resolution limits of these methods. Instead, the lengths and diameters of the connecting cilia from six *Xenopus* rods were determined from transmission electron micrographs, the average results of which are given in Table I. From these data, we derived an average CC cross-sectional area as a function of axial dimension that we then inserted into the cross-sectional area array at an axial position determined from visual inspection of the fluorescent image of the cell (Fig. S2). A complete quantitative description of the plasma membrane–delimited dimensions of the individual cell under investigation was thus generated.

Analysis of PAGFP concentration effects on estimation of D

The concentration of PAGFP in the rods examined was estimated as described in Peet et al. (2004). In brief, the average fluorescence of the brightest 5% of voxels in a cell was determined and assumed to represent the voxels with the least volume occupied by subcellular structures before photoactivation. The PAGFP concentration was then obtained with the following equation (cf. Peet et al., 2004):

$$[\text{PAGFP}]_{\text{cell}} = \frac{F}{K \cdot I_{\max} \cdot 10^{-ndf}}, \quad (\text{S29})$$

where F is the mean fluorescence of the brightest 5% voxels, I_{\max} is the intensity of the unattenuated 488-nm laser, ndf is the calibrated density of the neutral density filter used to attenuate the laser during cell imaging, and K is a system constant obtained from measurements with

recombinant protein. For calibration of rPAGFP concentration, we assumed an extinction coefficient of $\epsilon_{400} = 20,700$ (Patterson and Lippincott-Schwartz, 2002).

Does local binding significantly impact estimation of D_{PAGFP} in rod cells?

The range of PAGFP concentrations in the cells we examined spanned 2.3 decades, and yet D_{CC} did not correlate with PAGFP concentration (Fig. S3). This strongly argues against significant binding of PAGFP, although it does not rule out weak binding that may have a small impact on PAGFP diffusion.

Does self-crowding significantly impact estimation of D_{PAGFP} in rod cells?

We determined the level of self-crowding produced by the measured concentrations. The mean distance, d , between PAGFP molecules may be calculated as:

$$d = c^{-1/3}, \quad (\text{S30})$$

where c is the concentration expressed in molecules/distance³ (at the high end of the concentration range examined, $\sim 100 \mu\text{M}$, $d = 25.5 \text{ nm}$). Self-crowding does not appear to significantly affect diffusion of macromolecules until the volume fraction occupied by the molecules exceeds $\sim 10\%$ (See Dix and Verkman, 2008 and Zhou et al., 2008). GFP is an approximately barrel-shaped molecule with dimensions of $\sim 4.2 \text{ nm}$ long and $\sim 2.4 \text{ nm}$ in diameter, and thus occupies a volume of 19 nm^3 . The spacing of PAGFPs in the highest expressing cells we examined ($d = 25.5 \text{ nm}$) means that on average, each PAGFP is surrounded by a volume of $16,581 \text{ nm}^3$ within which no other PAGFP molecule resides, produc-

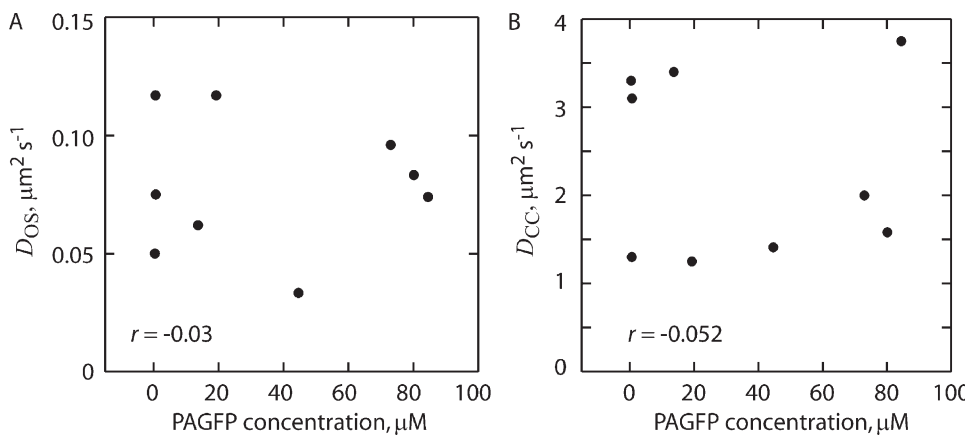


Figure S3. Test of the hypothesis that PAGFP diffusion coefficients correlate with PAGFP concentration. D_{OS} (A) and D_{CC} (B) values were plotted as a function of PAGFP concentration determined in the IS before photoconversion. Linearity of the relationships was assessed by computing sample correlation coefficients, r , which were found to be -0.052 and -0.03 for the CC and OS, respectively, indicating no correlation of D with concentration in either compartment.

ing a volume ratio of 0.1%. This clearly argues against self-crowding having a significant impact on the apparent PAGFP diffusion coefficients measured in rods.

Advection/diffusion model of soluble protein transport

Advection is the process of fluid flow caused by some generating force, such as vesicles being transported through the narrow CC lumen. An advective component may be introduced into Eq. 13 of Theory to yield the advection/diffusion PDE,

$$\frac{\partial c}{\partial t} = \frac{1}{A(z)} \frac{\partial \left(A(z) \cdot D(z) \cdot \frac{\partial c}{\partial z} \right)}{\partial z} - \frac{1}{A(z)} \frac{\partial (A(z)v(z)c)}{\partial z}, \quad (\text{S31})$$

where the additional term includes $v(z)$, the velocity of the advective flow in units of distance per time. The boundary and initial conditions, respectively, are

$$\begin{aligned} \frac{\partial c(z=l,t)}{\partial z} &= \frac{\partial c(z=L,t)}{\partial z} = 0 \\ c(z,t=0) &= c_0(z). \end{aligned} \quad (\text{S32})$$

Eqs. S31 and S32 were solved using the numerical MOL similarly as described for Eqs. 13–15 (Theory and see above). The magnitude of the flow velocity used, $1 \mu\text{m s}^{-1}$, was based on the vesicle transport rate necessary to supply the OS disc membranes with rhodopsin at a suitable density and the volume of the CC, derived from EM data in Table I, which provided a volumetric displacement as a function of time. Solutions were obtained for the system Eqs. S31 and S32 with varying values of D_{CC} and uniform initial concentration of transported species for all z over time long enough to achieve a steady state.

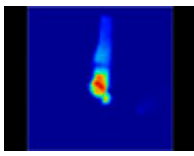
When D_{CC} was large ($>10 \mu\text{m}^2 \text{s}^{-1}$), the steady-state concentration distribution was similar to that found experimentally and with that of the diffusion-only model (uniform in the OS and IS compartments); thus, advection had little effect on transport. If D_{CC} was equal to the value estimated from the diffusion-only model ($2\text{--}3 \mu\text{m}^2 \text{s}^{-1}$), the steady-state concentration in the OS compartment exceeded that in the IS by 1.4–1.6-fold. For small D_{CC} values ($\leq 1 \mu\text{m}^2 \text{s}^{-1}$), the concentration in the OS compartment exceeded that in the IS from 2.6-fold up to the case where nearly all of the mass of the transported species collected in the OS. Thus, in the presence of diffusion and advection in the IS to OS direction, the concentration of PAGFP is predicted to be nonuniform, with higher concentrations predicted for the OS compartment. This result is consistent with a straightforward expectation based on an analysis of the flux of PAGFP through the CC. At steady state, there can be no net flux through the CC, and so throughout the CC we must have

$$q(z) = -vc(z) + D_{\text{CC}} \frac{dc}{dz} = 0, \quad (\text{S33})$$

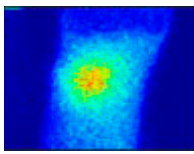
where v is the advective velocity. The solution of this equation predicts that the concentration of the diffusing species on the OS side of the CC (c_{OS}) is related to the that on the IS side (c_{IS}) by

$$c_{\text{OS}} = c_{\text{IS}} \exp\left[\frac{(z_{\text{OS}} - z_{\text{IS}})}{D_{\text{CC}} / v}\right]. \quad (\text{S34})$$

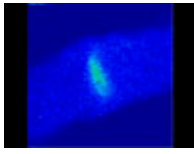
(Note that at steady state, concentrations within each of the OS and IS compartments must be uniform, although they are not necessarily equal.) The steady-state predictions of the advective/diffusion model (Eqs. S31 and S32) agree to within a few percent of the prediction of Eq. S34.



Video 1. PAGFP equilibration throughout rod photoreceptor cytoplasm. Frames acquired at 10-s intervals. Video playback at 10 frames per second.



Video 2. PAGFP diffusion in the IS. Frames acquired at 6.3 frames per second. Video playback at 10 frames per second.



Video 3. PAGFP diffusion in the OS. Frames acquired at 6 frames per second. Video playback at 10 frames per second.

REFERENCES

- Calvert, P.D., J.A. Peet, A. Bragin, W.E. Schiesser, and E.N. Pugh Jr. 2007. Fluorescence relaxation in 3D from diffraction-limited sources of PAGFP or sinks of EGFP created by multiphoton photoconversion. *J. Microsc.* 225:49–71. doi:10.1111/j.1365-2818.2007.01715.x
- Carslaw, H.S., and J.C. Jaeger. 1959. Conduction of Heat in Solids. Second edition. Oxford University Press, New York. 510 pp.
- Dix, J.A., and A.S. Verkman. 2008. Crowding effects on diffusion in solutions and cells. *Annu Rev Biophys.* 37:247–263. doi:10.1146/annurev.biophys.37.032807.125824
- Patterson, G.H., and J. Lippincott-Schwartz. 2002. A photoactivatable GFP for selective photolabeling of proteins and cells. *Science* 297:1873–1877. doi:10.1126/science.1074952
- Peet, J.A., A. Bragin, P.D. Calvert, S.S. Nikonorov, S. Mani, X. Zhao, J.C. Besharse, E.A. Pierce, B.E. Knox, and E.N. Pugh Jr. 2004. Quantification of the cytoplasmic spaces of living cells with EGFP reveals arrestin-EGFP to be in disequilibrium in dark adapted rod photoreceptors. *J. Cell Sci.* 117:3049–3059. doi:10.1242/jcs.01167
- Polyanin, A.D. 2001. Handbook of Linear Partial Differential Equations for Engineers and Scientists. Chapman & Taylor & Francis, London. 1544 pp.
- Schiesser, W.E. 1991. The numerical method of lines: integration of partial differential equations. Elsevier Academic Press, New York. 326 pp.
- Schiesser, W.E., and G.W. Griffiths. 2009. A compendium of partial differential equation models: method of lines analysis with MATLAB. Cambridge University Press, New York. 474 pp.
- Zhou, H.X., G. Rivas, and A.P. Minton. 2008. Macromolecular crowding and confinement: biochemical, biophysical, and potential physiological consequences. *Annu Rev Biophys.* 37:375–397. doi:10.1146/annurev.biophys.37.032807.125817